Layer 5 Martinotti cell activation reduces pyramidal cell population plasticity and improves fine motor function

Anna Velica[1]*, Thawann Malfatti[1]*, Jéssica Winne[1,2], Barbara Ciralli[1], Katharina Henriksson[1], Ingrid Nogueira[2], Evridiki Asimakidou[1,3], George Nascimento[2]#, Richardson Leao[2], Klas Kullander[1]

* equal contribution, # deceased 2022

[1]Department of Immunology, genetics and pathology, Uppsala University, Uppsala, Sweden.

[2]Brain Institute, Federal University of Rio Grande do Norte, Natal/RN, Brazil.

[3]Department of Clinical Neurosciences, University of Cambridge, CB2 0QQ, United Kingdom.

Klas kullander
klas.kullander@igp.uu.se

Highlights

- Chrna2+ Martinotti cells (Mα2) in primary motor cortex layer 5 receive direct input from thalamic nuclei and substantia innominata.
- Overexcitation of Mα2 cells reduces plasticity in pyramidal cell assemblies and induces premature activation of leader pyramidal cells during relearning.
- Loss-of-function and activity modulation experiments establish a role for Mα2 cells in execution of fine motor functions.

Abstract

During motor activity and motor learning, pyramidal cells in the motor cortex receive inputs from local interneurons as well as deeper structures. These signals funnel into pyramidal cells in the primary motor cortex that in turn feed commands to spinal circuits for execution. Here we show that layer 5 Chrna2 Martinotti cells receive direct input from thalamic nuclei, and that their genetic ablation results in disturbed fine motor functions. Activation of these layer 5 Martinotti cells during training reduces pyramidal cell plasticity, e.g. tuning, temporal patterning and assembly configuration. Moreover, in mice that had already learned a reach-and-grasp (prehension) task, Martinotti cell activation resulted in improved prehension. This work indicates that activation of layer 5 Martiotti cells reduces pyramidal cell assembly plasticity during learning, facilitating preservation of already acquired motor skills.

Keywords: Martinotti alpha 2 cell; Assemblies; Motor function; Plasticity

Introduction

Refined control of limb movement is crucial to perform essential behaviors such as building shelter, reaching for objects and exploring food. Several cortical areas contribute with various components to control and coordinate limb movements [1]. To initiate a voluntary movement, information is relayed from processed sensory information and command centers to circuits in the motor cortex, where the intended motor sequence is processed. The primary motor cortex (M1), which processes motor plans involving proximal and distal joints [2], delivers commands to spinal cord neurons to execute motor behaviors [3]. Upper motor neurons in M1 each have their muscle field [4] and act together to produce coordinated movements.

How the cortex is involved in motor learning and the execution of learned movements is still under debate. Most studies agree that cortical processing is necessary for the initiation of a learned motor sequence [5, 6, 7], but it remains unclear whether cortical processing is necessary for its execution. For example, a study used lesions and a lever pressing task to show that the rodent motor cortex is required for learning, but not for the execution of movements [8]. However, the use of optogenetic mid-movement activation of local inhibitory interneurons in the motor cortex could pause the execution of a learned movement, providing contradictory data [9]. Cortical excitatory and inhibitory interneurons serve as an interface between sensory inputs and motor commands and can thus provide entry points for the congregation of direct sensory input and processed information from the prefrontal cortex, to achieve the most purposeful movement at any given moment. Identifying the function and connectivity of specific

interneuron populations within M1 is an important step towards disentangling the neuronal circuits that control and modulate motor function.

Martinotti cells (MCs) are inhibitory interneurons, mainly found in neocortical layer 3 and 5 [10], typically express the neuropeptide somatostatin (SST), and project to layer 1 where they form synapses onto the distal dendrites of cortical pyramidal cells [PCs; 11]. The close location and functional relationship to PCs imply that MC inhibition plays an important role in shaping the output signal from PCs in the cortex to subcortical structures such as the spinal cord. Indeed, within neuronal circuits, MCs interact with layer 5 PC dendrites [12] and can themselves be activated by a single PC [13]. Network activity recruits MCs [14] and they can mediate a frequency dependent disynaptic inhibition between PCs [15]. There are several studies investigating the connectivity and functional role of SST-expressing interneurons [16, 17]. However, in the cortex, SST is expressed in a variety of interneuron populations including large basket cells, double-bouquet cells, long-range GABAergic projection cells, bitufted cells, fanning-out MCs and T-shaped MCs [10, 18, 19]. In fact, only around 50% of SST interneurons are MCs [20] and MCs are found in all cortical layers except for layer 1 [21]. Recently it has been shown that more specific genetic markers can subdivide SST interneurons and MCs into subtypes that reside in different cortical layers and exhibit different morphologies and axonal projection patterns [22, 23]. In mice, a subset of T-shaped MCs (herein referred to as Mα2 cells) located in layer 5b, expressing the cholinergic receptor nicotinic alpha 2 subunit (Chrna2), send inhibitory projections selectively to thick-tufted type A pyramidal tract PC where they can reset and synchronize PC activity in a frequency-dependent manner [24, 23]. These findings suggest that Mα2 cells are important for coordinated PC activity, which is involved in cortical information processing, not least in the M1. However, the role of Mα2 cells in motor commands and how their activity might influence PC activity to learn and produce purposeful motor behaviors is not understood.

To probe the possibility that Mα2 cells partake in motor processing, we used monosynaptic retrograde tracing combined with immunolabeling and found that Mα2 cells receive inputs from thalamic and cholinergic nuclei. Further, we evaluated skilled forelimb motor learning in a prehension task during chemogenetic activation of Mα2 cells, while simultaneously recording local field potentials, to examine the influence of Mα2 cells on cell population dynamics, and miniscope recordings, to decode single PC activity relative to the population. We then found that overexcitation of Mα2 cells increased motor performance of an already acquired skill, and reduced plasticity in PC assemblies during retraining.

Materials and methods

Animals

All animal procedures were approved by the local animal research ethical committee (Uppsala djurförsöksetiska nämnd) and followed the Swedish Animal Welfare Act (Svensk författningssamling (SFS) 2018:1192), The Swedish Animal Welfare Ordinance (SFS 2019:66) and the Regulations and general advice for laboratory animals (SJVFS 2019:9, Saknr L 150). Ethical permit number: 5.8.18-08463/2018, 5.8.18-08464/2018 and 5.8.18-07526/2023. Chrna2-Cre mice, produced and bred in our own facility [25], were crossed with either C57BL/6J (Taconic, Denmark), GT(ROSA)26Sortm14(CAG-tdTomato)Hze [RRID:IMSR_JAX:007914, 26] or GT(ROSA)26Sortm1.1(CAG-EGFP)Fsh/Mmjax [RRID:MMRRC_032037-JAX, 27] mice and the offspring were genotyped in house for the presence of the Chrna2-Cre allele and/or the tdTomato allele and the EGFP allele. The following primers were used: Chrna2-Cre 5'-gacagccattttctcgcttc-3' (forward) and 5'-aggcaaattttggtgtacgg-3' (reverse); tdTomato 5'-ctgttcctgtacggcatgg-3' (forward) and 5'-ggcattaaagcagcgtatcc-3' (reverse); EGFP 5'-gacgtaaacggccacaagttc-3' (forward) and 5'-cttctcgttggggtctttgct-3' (reverse). The Chrna2-Cre, tdTomato and EGFP allele were kept heterozygous. Animals were housed with littermates in approximately 501 cm2 individually ventilated cages (up to 5 animals/cage) with bedding and enrichment (a carton house and paper tissues), kept in a 12-h light on/light off cycle (6 a.m.–6 p.m.), and maintained at 21 ± 2 °C with a humidity of 45-64%. Animals were provided food (diet pellets, Scanbur, Sweden) and tap water ad libitum, except for when food was restricted for behavioral testing (see single pellet prehension task further down). After lens or electrode implant surgery, animals were housed individually to decrease risk of implant detachment. Mice were 6-25 weeks old at the start of experiments. Chrna2-Cre$^{tg/wt}$ and Chrna2-Cre$^{wt/wt}$ (Cre-negative littermates designated "controls") were used. Chrna2-Cre$^{tg/wt}$-tdTomato$^{lx/wt}$ mice (and Cre-negative littermates, Chrna2-Cre$^{wt/wt}$-tdTomato$^{lx/wt}$; controls) were only used for experiments with Cre-dependent caspase3-induced apoptosis. Chrna2-

Cre$^{tg/wt}$-EGFP$^{lx/wt}$ mice were only used in the tracing experiments. Female mice were used in the behavioral experiments, except for in the miniscope recordings in which male mice were used. For the tracing experiments both female and male mice were used. Throughout the paper, control mice refer to Cre-negative littermates that have received the same treatment as Cre-positive mice.

Viral injections

Mice were sedated with 1-4% Isoflurane (Baxter). Analgesia was given subcutaneously; 2 mg/kg bupivacaine (Marcain, AstraZeneca), 5 mg/kg carprofen (Norocarp vet, N-vet or Rimadyl Biovis vet) and 0.1 mg/kg buprenorphine (Vetergesic vet, Ceva). A midline incision was made in the scalp, muscles and periosteum were removed using 3% hydrogen peroxide (Sigma-Aldrich) and a hole (1 mm in diameter) was drilled at the site of injection (coordinates relative to bregma: AP 0.8 mm, ML 1.5 mm and DV -1.3 mm) with a hand-held drill. The injection coordinates targeted the forelimb area of the M1. The injection coordinates were chosen based on the Mouse Brain Atlas [28], as well as previous studies mapping the motor cortex [29, 30].Viral vectors (for more information see below for each experiment) were injected using a 10 μl Nanofil Hamilton syringe (WPI, USA) mounted on a stereotaxic frame. Ten minutes post injection the needle was slowly withdrawn from the brain and the wound was stitched with resorbable sutures (Vicryl rapide, Ethicon, 6-0). Mice were then left to recover for 2-4 weeks before any behavioral experiments were initiated. Viral transduction was confirmed by post-hoc histological analysis of brain sections.

For monosynaptic retrograde tracing experiments, 14 mice (9 Chrna2-Cre$^{tg/wt}$, 1 Chrna2-Cre$^{tg/wt}$;EGFP:loxP$^{lx/wt}$ and 4 Chrna2-Cre$^{wt/wt}$) were injected unilaterally in the right hemisphere with 500 nl of the adeno-associated virus (AAV) AAV8-hSYN-FLEX-TVA-E66T-P2A-GFP-P2A-oG-WPRE [LOT BA-229a: viral titer 3.98 x 1012 VG/ml, LOT BA-229b: viral titer 7.20 x 1012 VG/ml, Charité, Germany 31] and seven days later with 500 nl of the ΔG-rabies virus, pseudotyped EnvA, mCherry (BRVEnvA-1o: viral titer: 1.00 x 108 VG/ml, BRVEnvA-1n: viral titer: 1.4 x 108 VG/ml, BRVEnvA-1s: viral titer 3.4 x 108 VG/ml, Charité, Germany). The speed of the injections was 100 nl/min. Seven to ten days after the rabies virus injection, the animals were transcardially perfused and the tissue harvested.

For Cre-dependent caspase3-induced apoptosis, 14 female mice (7 Chrna2-Cre$^{tg/wt}$-tdTomato$^{lx/wt}$; 7 Chrna2-Cre$^{wt/wt}$-tdTomato$^{lx/wt}$) were injected bilaterally with 750 nl of AAV5-FLEX-TACASP3-TEVP (viral titer: 4.6 x 1012 VG/ml, batch #AV5760F) at a speed of 100 nl/min and were used for behavioral experiments. Two additional animals were injected unilaterally in order to check the percentage of neuronal ablation comparing the injected to the non-injected side.

For chemogenetic activation during local field potential (LFP) recordings, 14 female mice (7 Chrna2-Cre$^{tg/wt}$; 7 Chrna2-Cre$^{wt/wt}$) were injected bilaterally with 300 nl of AAV9-hSyn-DIO-hDM3q-mCherry (Addgene, LOT 44361-AAV9, viral titer 2.3 x 1013 GC/ml) diluted in 300 nl sterile saline (9 mg/ml, Fresenius Kabi, Sweden) at a speed of 200 nl/min.

For repetitive chemogenetic activation during training of the single pellet prehension task, 21 mice (10 Chrna2-Cre$^{tg/wt}$; 11 Chrna2-Cre$^{wt/wt}$) were injected bilaterally with 300 nl of AAV9-hSyn-DIO-hDM3q-mCherry (Addgene, LOT 44361-AAV9, viral titer 2.3 x 1013 GC/ml) diluted in 300 nl sterile saline (9 mg/ml, Fresenius Kabi, Sweden) at a speed of 200 nl/min.

For calcium imaging of pyramidal cell activity, 8 mice (5 Chrna2-Cre$^{tg/wt}$; 3 Chrna2-Cre$^{wt/wt}$) were first injected bilaterally with 300 nl of AAV9-hSyn-DIO-hDM3q-mCherry (Addgene, LOT 44361-AAV9, viral titer 2.3 x 1013 GC/ml) diluted in 300 nl sterile saline (9 mg/ml, Fresenius Kabi, Sweden) at a speed of 200 nl/min. One week post injection, the mice were injected unilaterally in the right hemisphere with 600 nl of AAV9-CamKII-GCaMP6f-WPRE-SV40 (Addgene viral prep # 100834-AAV9), at a speed of 200 nl/min. One week post-injection of AAV9-CamKII-GCaMP6f-WPRE-SV40, the mice underwent surgery for lens implantation (see Lens implantation below).

Electrode array assembly and implantation

For local field potential (LFP) experiments, mice were injected with AAV9-hSyn-DIO-hDM3q-mCherry (see viral injections above) bilaterally three weeks before electrode implantation surgery. Tungsten insulated wires of 35 μm diameter (impedance 100-400 kΩ, California Wires Company) were used to manufacture 2x5 arrays of 10 tungsten wire electrodes. The wires were assembled to a 16 channel custom made printed circuit board and fitted with an Omnetics connector (NPD-18-VV-GS). Electrode wires were spaced 200 μm and the array was implanted into the right hemisphere of the M1. Surgery preparation was performed as described for viral injection, and four small craniotomies were done in a square at coordinates AP

0.70 mm, ML 1.25 mm; AP 0.70 mm, ML 2.25 mm; AP 1.0 mm, ML 1.25 mm; and AP 1.0 mm, ML 2.25 mm; to make a cranial window were the electrodes were slowly inserted at DV -1.30 mm. Four additional craniotomies were drilled for the placement of anchoring screws (AgnThos, MCS1x2), where the screw placed over the cerebellum served as reference. The electrode implant was fixed to the skull with dental cement (Tetric EvoFlow) around the anchor screws. After surgery, the mice were monitored until awake, housed individually and allowed to recover for one week before recordings.

Lens implantation

The procedure was initially identical to the viral injections, but instead of injecting a virus, a prism lens (CLH type glass, lens diameter 1.0 mm, prism size 1.0 mm, total length of lens+prism 3.68±0.156 mm, working distance 0.3 mm, enhanced aluminum and SiO2 protective coating, Go!Foton, USA) combined with a relay GRIN lens (Imaging Focusing Rod Lens, diameter 2.0 mm, working distance at infinity) for recordings of cortical layer 5 was implanted unilaterally using the stereotaxic frame. To implant the prism lenses, the tip of a dissection knife was inserted 0.3 mm into the cortex for three minutes before the lens was lowered into the cortex with the tip 0.3 mm lateral and -0.5 mm dorsoventral to the viral injection coordinates. The lens was fixed to the skull and anchor screws with cyanoacrylate glue (OptiBond, Kerr Dental). Silicon glue (Kwik-Sil, World Precision Instruments) was added to protect the lens from mechanical damage in between experiments. Mice were treated with Enrofloxacin 5 mg/kg (Baytril) for two days pre-surgery and seven days post-surgery. Two to three weeks post implantation the mice were again anesthetized, the scalp incised, and the baseplate (used to attach the miniscope during recordings) was mounted on top of the skull with cyanoacrylate glue.

Drug preparation

The most commonly used chemogenetic agonist is clozapine-N-oxide (CNO), however, it has been suggested that the main effect on the engineered receptors, after systemically administered CNO, is mediated by back-converted clozapine [CLZ; 32, 33]. Since the conversion rate might differ between individuals [34], we chose to use low dose CLZ for chemogenetic experiments. A stock solution was made from 1 mg of CLZ (Hello Bio, batch E0697-1-1) (CLZ) dissolved in 40 μl dimethyl sulfoxide (DMSO, Sigma-Aldrich). The stock solution was kept at room temperature for the entire set of experiments. The working solution given to the mice was made fresh daily; 2 μl of the stock solution were diluted in sterile saline to a final drug concentration of 1 μg/ml. The mice then received 0.01 mg/kg CLZ intraperitoneally (i.p.).

Single pellet prehension task

The single pellet prehension protocol consisted of handling, habituation, training and test sessions. The handling and habituation were performed the same way throughout all experiments, while the number of training and test sessions varied based on the experimental design (see below for more information about each experimental group). During handling, each mouse was placed on the body and hands of the experimenter for five minutes during two consecutive days and sugar pellets (non-pareille, Dr.Oetker) were inserted in the home cages after handling. For habituation, after completed handling, animals were placed inside the test arena for ten minutes and allowed to freely behave with sugar pellets on the floor of the arena during two consecutive days. The arena consisted of an acrylic rectangular box of dimensions 22 cm x 9 cm x 20.5 cm with a vertical slit (0.5 cm wide) in one of the narrower walls. In front of the slit, an elevated (2cm) plate was attached to the outer wall of the arena. On the third day of habituation, mice were presented sugar pellets on a spoon, outside the slit of the arena, which they were allowed to retrieve with their tongues. Following habituation, the mice underwent ten minutes long test sessions every other day. All test sessions were performed after 15-20 hours of food restriction, starting at 5 p.m. the previous day. After the test session, the mice were returned to their homecage with free access to food and water. For all mice, the initial sessions were performed with spoon aided pellet delivery, to make it easier for mice to understand that they should reach for the pellet. The spoon was initially placed closer to the opening of the slit to increase success rate and motivation to perform the test. As the mice reached more, the spoon was gradually moved further away from the slit untill it was at the same distance as a fixed position on the plate outside the slit. After the fifth session, the pellet was presented on the fixed position on the plate, instead of on the spoon. The pellet was placed to the right of the slit opening, forcing the mice to reach with their left paw. The female experimenter was blinded regarding mouse genotype during the test. The behavior was recorded from the front using a high-speed camera (Panasonic high-speed camera, HC-V750) at 1920x1080 px fixed at 50 FPS.

For the caspase3 induced apoptosis group, af-

ter completing handling and habituation, 13 mice (7 Chrna2-Cre$^{tg/wt}$-tdTomato$^{lx/wt}$ and 6 Chrna2-Cre$^{wt/wt}$-tdTomato$^{lx/wt}$) were trained to take pellets from a spoon through the slit during four sessions, then trained to take pellets from the fixed position on the plate during three sessions. One mouse did not reach for pellets on the seventh session, and was therefore excluded. 12 mice (6 Chrna2-Cre$^{tg/wt}$-tdTomato$^{lx/wt}$ and 6 Chrna2-Cre$^{wt/wt}$-tdTomato$^{lx/wt}$) were selected and received viral vector injections (AAV5-FLEX-TACASP3-TEVP), followed by five more test sessions, starting at four weeks post-injection.

For the LFP group, 14 mice (7 Chrna2-Cre$^{tg/wt}$; 7 Chrna2-Cre$^{wt/wt}$) were used. After completing handling and habituation, the animals were trained during four sessions (session 1-4) to take pellets from a spoon through the slit, then trained for three sessions (session 5-7) to take pellets from the fixed plate through the slit. One that did not reach for pellets in the seventh session was excluded. 13 mice (6 Chrna2-Cre$^{tg/wt}$ and 7 Chrna2-Cre$^{wt/wt}$) were selected and received viral vector injections (AAV9-hSyn-DIO-hDM3q-mCherry), followed by six test sessions (session 8-13) with the headstage connected for LFP recordings four weeks post injections The LFP signal was recorded with a 16-channel Intan RHD 2132 headstage connected to an Intan RHD2132 amplifier board by a thin flexible wire. Mice were briefly anesthetized with isoflurane in order to connect the headstage, then allowed to fully recover and placed inside the arena. Afterwards, mice were disconnected from the headstage and returned to their homecage. In the first three sessions after viral injections (session 8-10) the mice received 0.9 % NaCl i.p. 45 minutes before the start of the recording. In the last three sessions (session 11-13) the mice received 0.01 mg/kg CLZ i.p. 45 minutes before the start of the recording.

For the group with repetitive Mα2 cell activation during learning, 21 mice (10 Chrna2-Cre$^{tg/wt}$; 11 Chrna2-Cre$^{wt/wt}$) were injected with viral vectors (AAV9-hSyn-DIO-hDM3q-mCherry). Three to four weeks after viral injection, the handling and habituation was started. After habituation, the mice underwent 11 test sessions. 45 minutes before the start of each session, the mice were injected with 0.01 mg/kg CLZ i.p.. The first five sessions, the animals reached through the slit for pellets placed on a spoon. After five minutes in the fifth session, the pellet was instead placed on a fixed position on the plate, and the mice were encouraged to reach for it for five more minutes (session 6). The following five sessions (session 7-11), the mice reached for the pellet in the fixed position on the plate during ten minute long sessions. Mice with no reaches in more than three sessions were excluded from the analysis, which resulted in exclusion of one Chrna2-Cre$^{tg/wt}$ mouse and three Chrna2-Cre$^{wt/wt}$ mice. Three Chrna2-Cre$^{tg/wt}$ mice were excluded due to no DREADD expression on post hoc tissue analysis.

For the miniscope group, 8 mice (5 Chrna2-Cre$^{tg/wt}$; 3 Chrna2-Cre$^{wt/wt}$) underwent viral injections and lens implant. 2 Chrna2-Cre$^{tg/wt}$ did not have any detectable GCaMP6f expression (checked with the miniscope under anesthesia before baseplate fixation), so they were excluded before the baseplate fixation step. The handling was started two to five weeks after lens implantation, followed by one additional habituation step in which the mice were habituated to the miniscope. The mice were then sedated with 1-4% isoflurane for two to five minutes while the miniscope was mounted on the baseplate and thereafter placed in a circular arena (diameter 45 cm) for 45 minutes, then returned to their homecage for 45 minutes and then once again placed in the circular arena for 45 minutes. After this habituation step the mice were sedated with 1-4% isoflurane for two to five minutes while the miniscope was disconnected from the baseplate. The mice were then returned to their homecage. A few days later, the mice underwent habituation to the single pellet prehension task as previously described, followed by six test sessions. 45-60 minutes before each test session the mice received 0.01 mg/kg CLZ i.p.. The miniscope was mounted on the baseplate on session 1, 2, 5 and 6. Only on those sessions, approximately 20 minutes after CLZ administration, the animals were sedated with 1-4% isoflurane for two to five minutes while the miniscope was mounted on the baseplate. After 20 minutes recovery from the sedation, the mice were placed in the prehension arena for ten minutes. In the arena, the cellular activity was recorded with the miniscope on session 1 (naive), 2 (trained), 5 (pellet presented on the spoon) and 6 (pellet placed on the fixed plate; retrained) and the behavioral activity was recorded with the video camera on session 1-6. A blinking LED light was used to synchronize the time stamps of the miniscope recordings with the behavioral videos. After the test, the mice were sedated with isoflurane in order to remove the miniscope from the baseplate. Session 1-5 were performed every other day, session 6 was performed on the same day as session 5 directly after session 5. Two mice, one control and one Chrna2-Cre+, had no prehensions in session 1 and were for this reason excluded. Data was recorded using a data acquisition device (DAQ) and a computer with Miniscope controller software installed. Focus of the miniscope was adjusted manually (300 μm range). Optimal laser power (around 30% of max brightness), imaging gain, and focal distance

was selected for each mouse and conserved across all sessions. The calcium signal was acquired at a frame rate of ≈ 20 frames per seconds, with the timestamp of each frame registered onto a separate file.

Automatic detection and classification of prehensions

For each pellet prehension task session, the positions of the pellet, both forepaws, thumb, index and middle fingers were tracked. The AI network used for tracking (see Software availability) was trained specifically for detection of the left paw and the three fingers at the prehension onset position (paw palm pointing inside, thumb pointing up and fingers pointing to the medial line), and a tracking likelihood threshold of 70% was achieved from prehension onset to grasp end. Therefore, prehensions were reliably detected as blocks where the tracking likelihood for the left paw and its three fingers was above 70%. Prehensions were classified as successful when the animal reached for the pellet, grasped the pellet and brought it to its mouth. Any other outcome (mice hitting the pellet but failing to grasp it; missing the pellet; grasping the pellet but dropping it before it reached the mouth; reaching for the pellet when no pellet was available) was considered a failed prehension.

Pasta Handling Test

The mice were tested in the pasta handling task, a quantitative assessment of skilled forelimb function, in order to measure forepaw dexterity [adapted from 30]. Mice were exposed to the pasta pieces (uncooked capellini pasta, 1.0 mm diameter, 2.6 cm length) in their home cage for five days to avoid neophobic reactions. Thereafter, the mice were habituated to eat inside the test arena (22 cm x 9 cm x 20.5 cm) for three days, without food restriction. After the habituation period, the mice were tested in the pasta handling test. The test consisted of sequential trials in which one pasta piece was delivered on the floor, in the center of the arena, for each trial. The behavior was recorded from the front using a high-speed camera (Panasonic high-speed camera, HC-V750) at 1920x1080 px fixed at 50 FPS. Test sessions were performed after 15-20 hours of food restriction, starting at 5 p.m. the previous day. Each session of ten minutes consisted of a maximum of five trials. To make it easier to see how the capellini strand would move while being consumed, each pasta piece received a food coloring mark on one half. The number of pasta drops and the time spent handling the pasta was then quantified by visual inspection. 9 mice (3 Chrna2-Cre$^{tg/wt}$-tdTomato$^{lx/wt}$; 6 Chrna2-Cre$^{wt/wt}$-tdTomato$^{lx/wt}$) bilaterally injected with AAV5-FLEX-TACASP3-TEVP were tested in the pasta handling task six weeks after viral injection and one week after the last pellet prehension task session.

Hanging Wire Test

The coordination and strength of the forepaws was tested by the hanging wire test, in which mice suspend their body by holding on to a single wire stretched between two posts 40 cm above the ground. The mice were placed on the middle of the wire hanging from its forepaws for three minutes. A paper bed was placed between the two posts to avoid injury when the mice fell. The time hanging on the wire and number of falls were quantified by visual inspection. 9 mice (3 Chrna2-Cre$^{tg/wt}$-tdTomato$^{lx/wt}$; 6 Chrna2-Cre$^{wt/wt}$-tdTomato$^{lx/wt}$) were used. Mice were injected with viral vectors (AAV5-FLEX-TACASP3-TEVP) bilaterally, then performed the single pellet prehension task, and after completion of the single pellet prehension task, they performed the pasta handling and finally the hanging wire test (six weeks after the viral vector injection).

LFP electrophysiology analysis

Square voltage pulses were used to trigger LFP and miniscope recordings; and to drive a red LED placed at the top right corner of the behavioral camera field of view. Therefore, behavioral video recordings were synchronized with the corresponding electrophysiological recording by detecting the LED onset in the video. LFPs from all 10 channels from each mouse were averaged, filtered using a 1-100Hz 2nd-order butterworth bandpass filter and sliced one second before and one second after each prehension onset. Slices were then grouped by prehension type (correct or incorrect) and averaged separately for each session.

In-vivo calcium imaging analysis

Miniscope videos were spatially downsampled 3x and motion-corrected, then cells signal was extracted using constrained nonnegative matrix factorization for microendoscopic data (CNMF-E) approach [35], and fluorescence traces were detrended by baseline subtraction (here referred as dF/F). Neuron identity was matched along multiple recordings through intersection over union metric and the Hungarian algorithm for optimal matching. Up to this step, all miniscope video analysis was done as implemented previously [36]. Prehension onset (time = 0 ms in all plots) was defined as the moment when the mouse's

paw forms the grasp position, flipping the palm inside, thumb pointing up and fingers pointing to the medial line, then neurons fluorescence traces were sliced 1s before and 1s after forepaw prehension onset, and slices were grouped by prehension accuracy (successful or failed) and averaged separately for each session. Only neurons that displayed a significant change comparing the before onset and after onset phases (ANOVA or Kruskal-Wallis, according to normality of distribution, evaluated using Shapiro's test) were kept for further analysis. For L5 pyramidal cells fluorescence peak latency analysis, traces for successful or failed grasps were separately averaged and normalized for each neuron, and neurons were sorted according to peak latency at successful grasps from each session. For PC response peak width, the width in seconds of the maximum response peak was calculated at half the peak prominence.

Assemblies were detected using independent component analysis with circular shifts, as implemented previously [37]. After removing neurons with no significant change comparing the before onset and after onset phases, only assemblies with 4 or more neurons and only neurons belonging to at least one assembly were kept for further assembly analysis. For calculating assembly area, neurons from the assembly were first sorted according to their cartesian angle relative to the center of the assembly, which is the average of neurons' (x,y) coordinates. Finally, the assembly area was calculated as the area of the polygon formed by the sorted neurons. Assemblies resilience was calculated by finding the assembly with highest neuronal composition intersection on the other sessions according to the following formula:

$$\frac{Size(Intersect_{Assembly1-Assembly2})}{Size(Assembly1)} + \frac{Size(Intersect_{Assembly1-Assembly2})}{Size(Assembly2)} * \left(\left(\frac{Size(Assembly2)}{Size(Assembly1)}\right) - 1\right) \quad (1)$$

such that resilience is within 0 (no intersection between assemblies) and 1 (exactly the same neurons forming both assemblies). To find assembly activity peaks, 1000 shuffles of activity of all neurons within an assembly on the time dimension were done, and activity peaks were considered as time samples where the sum of all neurons' real activity is larger than 95% of the sum of the shuffled neuronal activity, resulting in a rasterized activity (containing only 0 or 1 meaning inactive or active for each time point). Event histograms were calculated by slicing the assembly activity peaks in time windows of 2s around each prehension (1s before and 1s after onset), where each bin corresponds to a one time sample of 50ms, limited by the miniscope's 20 FPS recording speed. Assembly salience, a measurement of how relevant the activation (or silencing) of an assembly is within the prehension movement, was calculated as

$$\frac{ActivityPeaksInWindow}{TimeSamplesInWindow} - \frac{ActivityPeaksOutWindow)}{TimeSamplesOutWindow} \quad (2)$$

such that salience is within -100 (assembly is active every time sample out of the prehension window and not active on any time sample within the window) to 100 (assembly active in all time samples within the prehension window and at no time sample outside the window).

Tissue preparation and immunohistochemistry

To fix the tissue for post-hoc analysis, mice were transcardially perfused with phosphate buffered saline (PBS, Fisher BioReagents, CAT 10051163) followed by 4% formaldehyde (VWR Chemicals BDH®, CAT 9713.1000). The brains were dissected out and post-fixed in 4% formaldehyde overnight at 4°C, washed three times for ten minutes in PBS and then kept in PBS at 4°C until sectioning (a few hours or days). Before they were sectioned, the brains were embedded in 4% agarose in PBS. Sections were cut at a thickness of 70 μm using a Vibratome (Leica VT1000S) and then mounted with ProLongTM Gold Antifade Mountant (ThermoFisher Scientific, CAT P10144) or Fluoroshield (Abcam) on glass slides (Superfrost®Plus, Thermo Scientific). For some mice, six weeks after the injection of AAV9-hSyn-DIO-hDM3q-mCherry, CLZ 0.01 mg/kg was administered i.p. 135 minutes before transcardial perfusion. After sectioning these brains, the sections were washed in PBS and pre-blocked for one hour in 2% donkey serum (Biowest), 1% Bovine Serum Albumin (BSA, Sigma Aldrich), 0.1 % Triton®X-100 (Sigma Aldrich) and 0.05% Tween®20 (Sigma Aldrich) in PBS. The primary antibody, c-Fos(4)-G (goat polyclonal IgG, Santa Cruz Biotechnology, CAT K1314) or c-Fos (9F6) (Cell signaling, rabbit, #2250) and anti-mCherry (ThermoFisherScientific, 16D7, rat, M11217) were diluted 1:500 in 0.25% gelatin and 0.5 % Triton®X-100 in Tris-HCl buffered saline (TBS; 0.3% Tris, 0.8% NaCl and 0.02% KCl in mqH2O, pH 7.4) and added to the sections. After 48 hours of incubation at 4°C the sections were

washed with TBS and the secondary antibodies, donkey anti-goat A647 (ThermoFisherScientific A21447), donkey anti-rabbit A647 (ThermoFisherScientific A31573) and donkey anti-rat A488 (ThermoFisherScientific A21208) were diluted 1:500 in 0.25% gelatin and 0.5 % Triton®X-100 in TBS, added to the sections and incubated for 90 minutes at room temperature. The sections were washed with 0.1% Tween in TBS and distilled water before they were mounted on glass slides.

For retrograde tracing experiments the entire brain (cerebrum, cerebellum and brainstem) was sectioned, mounted and examined in a widefield microscope (Olympus BX61WI, Japan) with a 10x objective. For the control mice and the first four Chrna2-Cre+ mice, all GFP and mCherry positive cells were imaged (see "Imaging and post processing" for more information). For the following Chrna2-Cre+ mice used, the sections were first checked in the widefield microscope with a 10x objective before the sections were mounted, to find sections suitable for immunohistochemical analysis. The sections chosen for immunohistochemical analysis were then pre-blocked for two hours at room temperature in a blocking solution (3% donkey serum and 0.3% Triton®X in PBS) before they were incubated overnight (except for anti-vasoactive intestinal polypeptide and anti-somatostatin which were incubated for 72 hours) at 4°C on a rocking table with the primary antibodies diluted in the blocking solution. Thereafter, sections were washed with PBS three times for ten minutes before they were incubated for three hours at room temperature with the corresponding secondary antibody diluted 1:500 in the blocking solution. Then, sections were stained with 200 ng/ml DAPI (Sigma) in PBS for ten minutes. Finally, they were washed two times for ten minutes with PBS and mounted on glass slides. Primary antibodies: anti-GFP (Abcam, ab13970, chicken polyclonal, dilution 1:1000), anti-parvalbumin (Swant, PV27, rabbit, dilution 1:1000), anti-calbindin (Swant, CB38, rabbit polyclonal, dilution 1:1000), anti-calretinin (Swant, 7697, rabbit, dilution 1:1000, anti-choline acetyltransferase (Millipore, 2843074, goat, dilution 1:1000), anti-GABA (Sigma, A2502, rabbit, dilution 1:750), anti-somatostatin (Merck Millipore, clone YC7, rat, dilution 1:150), anti-vasoactive intestinal peptide (Thermofisher, PA5-78224, rabbit polyclonal, 1:1000). Secondary antibodies: goat anti-chicken A488 (Jackson ImmunoResearch 103-545-155), donkey anti-rabbit A647 (ThermoFisherScientific A32795), donkey anti-rabbit A647 (Invitrogen A31573), donkey anti-goat A647 (ThermoFisherScientific A21447), donkey anti-rat A647 (Invitrogen A48272), donkey anti-rat 488 (Invitrogen A21208).

Imaging and image post processing

Most wide field images were acquired on a Zeiss Axio Imager Z2 (Zeiss, Germany) with a 10x objective (effective NA 0.45), a colibri LED 7 and Zen blue software (Zeiss, Germany), using a multi-band bandpass filter (Zeiss, Germany) with the filter excitation wavelengths 370-400 nm, 450-488 nm, 540-570 nm, 614-647 nm, 720-750 nm and the filter emission wavelengths 412-438 nm, 501-527 nm, 582-601 nm, 662-700 nm, 770-800 nm for the fluorophores DAPI, Alexa 647 and GFP and a single-band bandpass filter (TxRed-4040C-ZHE-ZERO, Semrock) with the excitation wavelengths 540-552 nm and emission wavelengths 590-4095 nm for mCherry. The light source used for the different fluorophores was LED-module 385nm for DAPI, LED-module 630 nm for Alexa 647, LED-module 475 nm for GFP and LED-module 567 nm for mCherry. Some images were taken using an Olympus BX61WI fluorescence microscope (Olympus, Japan) with a 10x (effective NA 0.40) objective and a Volocity 4.1.0 software (Quorum Technologies) or a Zeiss LSM700 confocal microscope (BioVis facility, Uppsala University). Brightness and contrast were adjusted in the Fiji software [38], equally for the whole image and without obscuring any data.

Coordinates relative to bregma were identified based on the Mouse Brain Atlas [28]. Abbreviations and brain region identification followed the Allen brain atlas data portal (http://atlas.brain-map.org). Cell counts were done manually with the Fiji counter plugin and the cell diameter was measured manually in Fiji. For cortical layer counts DAPI was used to distinguish the layers. For calculating cell distance to cortex surface, two points were marked at the cortex surface, then a line was interpolated from these points for each coronal image, and cell dorsoventral (DV) coordinates were calculated as the shortest euclidean distance between each cell and the interpolated line. For the visualization of cell distance to cortex surface, the traced cells were divided in three different groups; by the injection site (on brain sections with starter cells), anterior (>0.5 mm anterior of the most anterior starter cell) and posterior (>0.1 mm posterior of the most posterior starter cell). The probability density function of cells was calculated by performing a bidimensional gaussian kernel density estimate on the cell coordinates (ML x AP or AP x DV) interpolated 100 points on each axis. The cell diameter was manually measured in the Fiji software. For cell morphology classification, the cells were manually classified as interneurons (smaller oval or round cell body), pyramidal cells (more triangularly shaped cell body with a pronounced apical axon) or undetermined cells (slightly

out of focus or no traceable dendrites/axons).

For Chrna2, anti-GFP immunolabeling was performed, since the GFP signal in Chrna2Cre-EGFP mice was initially too weak. In Chrna2Cre-EGFP mice, it is difficult to distinguish double-positive traced cells co-expressing mCherry and GFP from starter cells, based on the method used. However, in the Chrna2Cre-EGFP mouse, there were 7 Chrna2/GFP and mCherry double-positive cells, of which at least 6 were classified as starter cells based on their location in cortical layer 5 by the injection site and based on their extensive dendritic staining compared to the surrounding GFP labeled Chrna2+ cells, indicating that they had a higher GFP expression after being transfected with the GFP-expressing helper virus. One Chrna2/GFP and mCherry double-positive cell was classified as a likely traced cell based on its location more than 1 mm away from the injection site.

Statistical analysis

Differences were evaluated using mixed-models ANOVA, with post-hoc Tukey' HSD (independent balanced factors) or t-test for pairwise comparisons. Where the data showed non-normal distribution, evaluated using Shapiro's test, ANOVA-type statistics [39, mixed models] or Scheirer-Ray-Hare (independent factors) were used for multiple factors; Kruskal-Wallis and Friedman's tests with F-ratios were used [40] for independent and dependent single factors, respectively; and post-hoc Mann–Whitney U or Wilcoxon signed-rank tests for independent and paired factors, respectively. Post-hoc multiple comparisons were adjusted by Holm correction, and statistical significance was conditioned to a false positive risk lower than $\alpha = 0.05$. Error bars represent standard error of the mean (s.e.m) for all figures. For all violin plots, the filled area represents the entire data range, and triangle markers represent means.

Software availability

LFP recordings were done using the Open-ephys GUI [41]. Calculations were done using Scipy [42], Numpy [43] and SciScripts [44], all plots were produced using Matplotlib [45] and schematics were drawn using Inkscape [46]. Cell fluorescence signals were extracted and processed from miniscope videos using CaImAn [36] and OpenCV [47]. Tracking of the mouse forepaw and fingers was done using DeepLabCut [48]. All scripts used for data analysis, including the DeepLabCut trained network, are available online (M1MartinottiOnMovement_2024 git repository; M1MartinottiOnMovement).

Results

Monosynaptic tracing of Mα2 cells revealed direct input from thalamic and cholinergic nuclei, as well as from cortical parvalbumin interneurons

We first aimed to identify presynaptic input to Mα2 cells using a G-protein deleted, Envelope A coated, rabies viral vector. The vector carries the mCherry fluorescent marker and requires an avian tumor virus receptor A (TVA) receptor to enter cells and an optimized glycoprotein (oG protein) to retrogradely cross a synapse [49, 50]. The TVA receptor, oG protein and a green fluorescent protein (GFP) were delivered into the forelimb area of the M1 by a Cre-dependent helper virus, following a simplified flowchart for control experiments [51, ; Figure 1A]. In control mice (n=4), no GFP+ cells were found and only an average of 1 mCherry+ cell was found at the proximity of the injection site, with no mCherry+ cells in distant brain regions (Figure 1B, Supplemental Table 1). In Chrna2-Cre+ mice (n=4), on average, 11 starter cells co-expressing GFP and mCherry were found in M1 by the injection site in cortical layer 5b (Figure 1C, Supplemental Table 1, n=3, average total number of traced mCherry+ cells, 799, n=4). Several traced cell somata had a pyramidal shape and were located in cortical layers 2/3 and 5 (Figure 1D). Most presynaptic cells were located in the ipsilateral cortex (94.8%, SD 2.5), with 72.1% (SD 8.5) of the traced cells located in the ipsilateral M1, 12.9% (SD 8.7) in the ipsilateral secondary motor cortex (M2) and 9.8% (SD 2.3) in the ipsilateral primary somatosensory cortex (S1). We also found cells in the ipsilateral thalamus (3.5%, SD 2.1), contralateral cortex (1.2%, SD 0.4), ipsilateral substantia innominata (0.19%, SD 0.1), ipsilateral globus pallidus externa (GPe; 0.19%, SD 0.2) and ipsilateral striatum (0.1%, SD 0.1; Figure 1E-F, Supplemental Table 2). Within the ipsilateral S1, 74.1% (SD 10.8) of the cells were located in the forelimb area, 16.6 % (SD 10.8) in the barrel field area, 6.8% (SD 10.8) in the mouth area and 2.5 % (SD 3.3) in the hindlimb area. Possibly, the direct connection from the S1 forelimb area could be important for minimizing delays in sensorimotor control and adjustments of skilled forelimb movements [52]. In the thalamus, there were 22 traced cells per animal (n=4, SD=15), located at Bregma -1.20 (SD 0.28). More specifically, the traced thalamic cells were found in the ipsilateral ventrolateral nucleus (94.1%), anteromedial nucleus (3.3%), posterior complex (1.3%), mediodorsal nucleus (0.7%) and ventral posterolateral nucleus (0.7%).

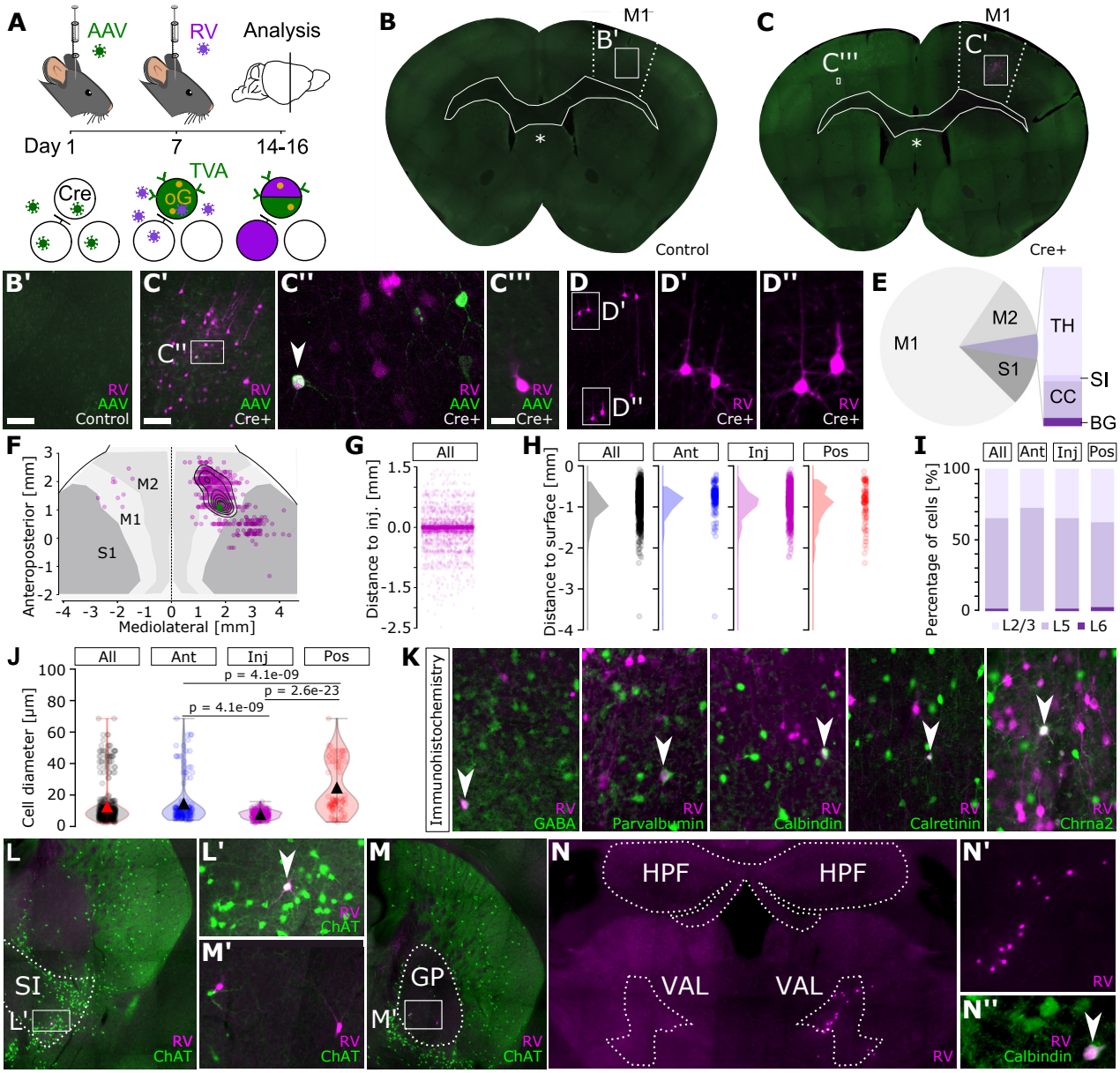

Figure 1: Retrogradely traced inputs to Mα2 cells in the primary motor cortex (M1) A) Schematic illustration of monosynaptic retrograde tracing using a Cre-dependent viral vector (AAV) carrying genes encoding the TVA-receptor (TVA), optimized G-protein (oG) and GFP together with an EnvA-pseudotyped G-protein deleted mCherry rabies virus (RV). B-C) Images of brain sections at the injection site, with AAV infected cells (green), starter cells (white) and traced cells (magenta) found in Chrna2-Cre+ mice (C) but not in control mice (B). Boxes indicate areas of enlargement seen in B', C' and C". * = corpus callosum. D) Pyramidal cells in M1 cortical layer 3 (D') and 5 (D"). E) Distribution pie-chart of presynaptic inputs of Chrna2-Cre+ cells. M2, secondary motor cortex; S1, primary somatosensory cortex; TH, thalamus; CC, contralateral cortex; SI, substantia innominata; BG, basal ganglia (globus pallidus externa and striatum). F) Density plot of the cortical traced cells in one mouse. Coordinates relative to bregma, injection site (green star). Cortical areas (M1, M2, S1) marked by gray shades. G) Anteroposterior spread from the injection site of all traced cortical cells compiled from 4 mice. H) Dorsoventral spread of traced cortical cells at the injection site (Inj), >0.5 mm anterior of the injection site in M2 (Ant) and >1 mm posterior of the injection site in S1 (Pos) (n=4 mice, n=1089; 819, 173 and 97 cells, respectively). I) Percentage of traced cells in different cortical layers at Inj, Ant and Pos. J) Diameter of traced cortical cells at Inj, Ant and Pos. K) Immunohistochemical stainings (green) of traced cells (magenta) in the cortex by the injection site demonstrate double-positive cells (arrowheads). L, M) Traced cell (arrowhead, magenta) in the L) ipsilateral substantia innominata and M) ipsilateral globus pallidus (SI and GP, delineated by dotted lines), ChAT+ cells (green). Box indicates area of enlargement in L' and M'. N) Traced cells in the ipsilateral ventral anterolateral complex of the thalamus (VAL). Hippocampal formation (HPF) and VAL are delineated by dotted lines. N', enlargement of the traced cells seen in N. N", a calbindin+ (green) traced cell (white, arrowhead) Scale bars: 500 μm in B and C, 200 μm in B', C', L, M and N, 100 μm in N', 20 μm in C" and N", and 40 μm in C"', D', D", K, L' and M'.

In the cortex, the number of cells was highest near the injection site, with 61.9% of the cells being located on sections within 100 μm from the starter cells. The traced cortical cells were ranging from 1.4 mm anterior of the

starter cells to 2.5 mm posterior (n=4, 3210 cells, Figure 1G, Supplemental Table 1) and had similar dorsoventral spread (n=2 mice) at the injection site (819 cells) as well as anterior of the injection site (173 cells), whereas more posterior cells had a bimodal dorsoventral spread (97 cells; Figure 1H). Accordingly, traced cells were predominantly found in cortical layer 2/3 (34.6%) and 5 (63.5%), with no cells in layer 4 (n=3 mice, 312 cells; 44 (Ant), 156 (Inj) and 112 (Post); Figure 1I). This explains the distribution of the dorsoventral spread, as the cells at the injection site and more anterior cells were located predominantly in M1 and M2 (where layer 4 is not present), while the posterior cells were located mostly in S1 (Figure 1F).

Based on their morphology, the cortical cells were classified as interneurons, PCs or undetermined cells. At the injection site, 11% of the cells were interneurons, 22% PCs and 67% undetermined. In contrast, 1 mm anterior or posterior of the injection site, 2% of the cells were interneurons, 66% PCs and 32% undetermined. To support our assessment, that the proportion of PCs increases farther away from the starter cells, we also measured cell diameters (n=2 mice, 300 cells), as an estimate of cell size and identity, and found that the distance from the starter cells had an effect on the cell diameter (Kruskal-Wallis, F(2,485)=116.349, p=5.4e-26). Cells at the injection site (on section with starter cells) were smaller than both more anterior (Mann-Whitney U, eff.size=0.296, p=4.1e-09) and posterior cells (Mann-Whitney U, eff.size=0.549, p=2.6e-23). The average cell diameter was 13.8 μm at the injection site (SD=3.5, n=300 cells from 2 animals), 15.7 μm 0.5-1 mm anterior (SD=4.4, n=134 from 4 animals), 19.1 μm >1 mm anterior (SD=6.9, n=32 from 2 animals) and 18.4 μm >1 mm posterior of the injection site (SD=4.7, n=100 cells from 4 animals, Figure 1J). This suggested that the distribution of cell types depended on the distance from the starter cells, with predominantly larger, presumably PCs, farther away, and a more mixed neuronal population, consisting of both PCs and interneurons, closer to the starter cells.

We next analyzed the identity of traced cells using immunohistochemistry. At the injection site, 2.5% co-expressed gamma-aminobutyric acid (GABA). However, farther away than 0.5 mm from the starter cells, none of the traced cortical cells were positive for GABA. As expected, this suggested that most traced cells were excitatory, presumably PCs. Further, inhibitory presynaptic cells were found close to the starter cells. Cortical inhibitory interneurons can be grouped into three major subclasses expressing PV, SST or the ionotropic serotonin receptor 5HT3a. The serotonin receptor population can further be divided into vasoactive intestinal polypeptide (VIP) and non-VIP interneurons [53, 54]. Most previous studies show that SST interneurons receive direct input from PCs and VIP interneurons [18, 55], but there are also studies showing direct input from PV interneurons [56]. However, subtypes of SST interneurons have different connectivity patterns [23], resulting in different functional properties [57]. We used markers for subpopulation of inhibitory interneurons to characterize the inhibitory input to Mα2 cells and found that, within 0.5 mm from the injection site, 4.2% of the traced cortical cells co-expressed parvalbumin (PV), 0.8% calbindin and 0.4% calretinin. In the Chrna2Cre-EGFP mouse, there were 7 GFP and mCherry double-positive cells, of which one was classified as a possible traced cell based on its location more than 1 mm away from the injection site (Figure 1K, Supplemental Table 3), and the rest were classified as starter cells. None of the traced cortical cells expressed SST, VIP or choline acetyltransferase (ChAT). Since we did not find any input from VIP interneurons, it is likely that Mα2 cells have different functional properties compared to other SST interneurons. To investigate potential cholinergic inputs to Mα2 cells, we performed immunostainings for ChAT and found positive immunostained traced cells in substantia innominata (2 out of 3 mCherry+ cells, Figure 1L). None of the traced cells in striatum (0 out of 3 mCherry+ cells) or GPe (0 out of 9 mCherry+ cells) co-expressed ChAT (Figure 1M). Previous studies have shown a direct connection from GPe to the frontal cortex in both rodents and primates [58, 59], and it is likely that such connections are also present in humans [60]. Since none of the traced GPe neurons were ChAT+, they are most likely inhibitory and spontaneously active [58, 59]. Whereas none of the immunostained traced cells in the thalamus expressed parvalbumin (0 out of 29 mCherry+ cells), a small fraction expressed calbindin (3 out of 20 mCherry+ cells), indicating that these are excitatory principal neurons [61, Figure 1N]. Taken together, our results show that Mα2 cells receive direct input from the basal forebrain, GPe and thalamus, as well as PCs and adjacent PV interneurons in the cortex.

Increased Mα2 cell activity affected calcium signal amplitudes in PCs during training

Considering the dual roles of the primary motor cortex as a motor control structure and a dynamic substrate that participates in motor learning [62], we were particularly interested in how PCs were affected by Mα2 cells in motor learning. To probe how increased activity of

Mα2 cells affects fine motor skills and motor learning we turned to chemogenetic activation using Designer Receptors exclusively activated by designer drugs [DREADDs; 63]. First, we validated that clozapine (CLZ) activated hDM3Gq transfected Mα2 cells (Supplemental figure 1). Next, a prehension task, in which mice are encouraged to reach for and grasp a sugar pellet, was used to evaluate fine motor functions and motor skill learning [64, 65, 66]. Most dendritic spines that correlate with learning are formed after the initial training session and are kept in the second training session [67]. Thus, we performed a set of recordings during a naive session for collection of data in untrained mice, as well as in a trained session to follow learning progression, and in a retraining session, during which a more challenging presentation of the pellet was introduced to follow relearning (Figure 2A-C). We turned to calcium imaging to analyze the contribution of increased Mα2 cell activity on individual PCs during training. The calcium signal in PCs was obtained using a viral vector with CamKII promoter driven expression of the calcium indicator GFP Calmodulin M13 peptide 6 fast (GCaMP6f). The increase in calcium levels corresponds to increased cell activity, and single spikes can only be indirectly estimated [68, 69, 70]. The emitted light was recorded in cortical layer 5 using an implanted optical lens and prism assembled to a miniscope [Figure 2A; 71, 72]. In the miniscope recordings, an average of 84.8 ± 14.2 PCs (n=4 mice; 2 ctrl, 133 and 68; 2 Chrna2-Cre+, 77 and 61) were detected. Analysis of calcium transients demonstrated that individual cell activities were readily identifiable and showed diversified activity profiles (Figure 2D-E). Cell activity was aligned to prehension onset (t=0), and the average PC population activity was measured across two distinct phases: one-second window before prehension (motor planning) and another one-second window during prehension (motor execution).

In the first session, we found an overall effect of genotype (ANOVA-type, F1-LD-F2 model F(1,inf)=11.68, p=1.9e-03; Figure 2F), indicating that overexcitation of Mα2 cells, i.e. increased inhibition, significantly decreased PC amplitude in naive mice. This decrease was not seen in the following training session, suggesting that this initial effect was compensated for. In contrast, we found an overall effect of genotype in the retraining session (ANOVA-type, F1-LD-F2 model F(1,inf)=6.58, p=2.1e-02; Figure 2F). Mice with overexcited Mα2 cells during retraining did not display the PC amplitude decrease observed in controls, hinting at a potential reduction in the plasticity of PCs upon Mα2 cell overexcitation. Further separating by prehension accuracy (successful or failed), this effect was stronger for successful prehensions, and an overall effect of phase was found, but no effect of genotype was found in this session (Supplemental text).

Increased Mα2 cell activity is related to earlier PC firing during retraining

Changes in sequential activation of PCs are linked to learning [73] thus, we next analyzed the temporal profiles of PCs, and identified the time point where they reached their maximum activity within the prehension window (Figure 3A). We compared the response peak latency between genotypes, sessions, prehension accuracy and phase. For each session, the activity for each neuron for all prehension types was averaged within the prehension window around the prehension onset and normalized (divided by its own maximum fluorescence). Individual neurons were sorted based on their latency to peak during successful prehensions (Figure 3B-H). We found a strong effect of prehension accuracy on the latency-to-peak distribution on all sessions and for neurons from both phases (ANOVA-type, F1-LD-F1 model F(1,inf)>=39.695; p<=3.0e-10; Figure 3I). These results indicate that neurons change their temporal activity pattern according to prehension accuracy, regardless of genotype, training session or the phase in which neurons reach their response peak. In the retraining session, PCs active before successful prehension onset displayed a premature response peak latency in Chrna2-Cre+ mice compared to control mice (n=104 control and 67 Chrna2-Cre+; Mann-Whitney U eff. size=0.257; p=9.2e-03; Figure 3J). This premature mean response was not found in failed prehensions (Figure 3J). Taken together, this analysis shows that increased Mα2 cell activity is related to premature PC firing, and that the temporal pattern shifts according to prehension accuracy regardless of genotype.

The width of the response peak measures the temporal specificity of the cell activation, with broader responses being less temporally specific, and vice versa. We evaluated the PCs peak width for all conditions (Supplemental figure 3), and found an interaction effect of genotype and training in the width of PC response peaks (ANOVA-type, F1-LD-F2 model F(2,inf)=3.288, p=3.8e-02), driven by the effect of genotype found in the naive and trained sessions (ANOVA-type, F1-LD-F1 model F(1,inf)>8.944, p<5.6e-03), but not in the retrained session. In addition, we found an interaction effect of genotype and accuracy (ANOVA-type, F1-LD-F2 model F(1,inf)=4.606, p=3.2e-02). Chrna2-Cre+ mice had sharper peak widths compared to controls in the naive session, and in the successful

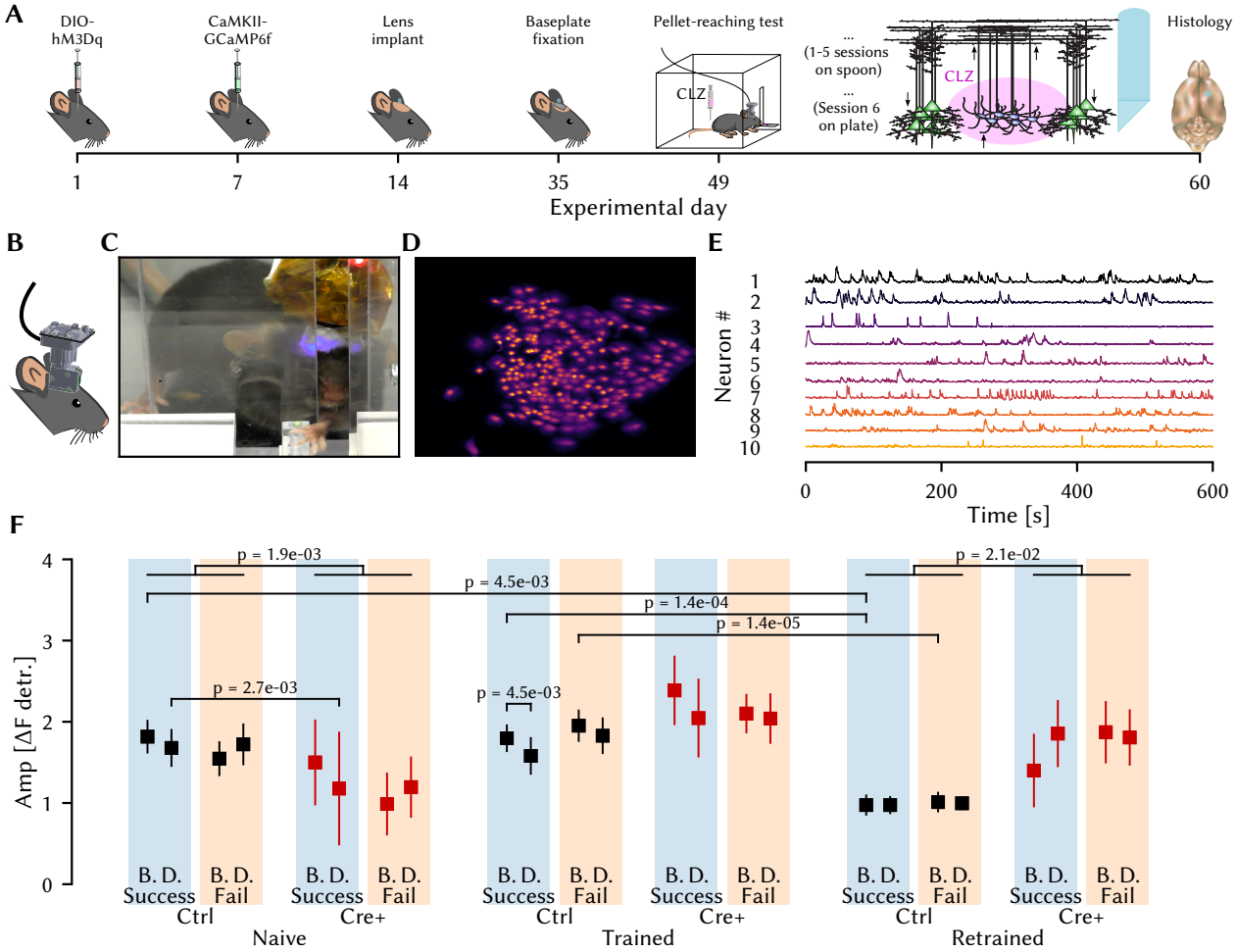

Figure 2: Mice with increased Mα2 cell excitability display decreased PC activity amplitude before training and increased PC activity upon retraining. A) Timeline of experiments showing viral injections, miniscope lens implantation, base plate fixation and pellet-reaching task. GCaMP6f fluorescence and forepaw movements were recorded in naive, trained and retrained sessions. B-C) Schematics (B) and photograph (C) of a mouse with the miniscope connected during prehension. D) Representative miniscope image of L5 pyramidal cells after cell detection. E) Ten representative example fluorescence traces from PCs. F) Average amplitude of PC activity represented as mean ± SEM, separated by session (naive, trained, retrained), genotype (control, black; Cre+, red), prehension accuracy (Success, successful prehensions, blue shade; Fail, failed prehensions, orange shade) and prehension phase (B., before; D., during prehension).

prehensions in the trained session (n=201, control; n=137, Chrna2-Cre+, Mann-Whitney U eff. size>0.147, p<2.7e-02; Supplemental figure 3D). Together, this analysis shows that mice with overexcited Mα2 cells display sharper responses than controls in naive and trained sessions.

Increased Mα2 cell activity resulted in PC assembly salience rigidity, area compaction, and increased resilience

We reasoned that examination of PC Hebbian assemblies may reveal how Mα2 cell activation influences cortical processing. Assemblies were identified according to similar cell firing using independent component analysis with circular shifts [ICA-CS; 74] during the entire 10 minute recording of a session, such that assembly detection is not affected by prehension accuracy (Figure 4A). We used either the naive or retraining session to identify assemblies containing at least four neurons, and excluded neurons that were not part of any assembly. Motor training is associated with a selective increase in connectivity among task-related PCs [75]. On a PC population level, we investigated this through assembly salience. Assembly salience is here defined as the activity of the assembly within the prehension window in relation to its own activity outside the prehension window (Figure 4B), ranging from -100 (no prehension-related assembly activity and assembly fully active outside the window) to 100 (assembly is fully active within the window and has no activity outside the window). Salience data varied from -2.04 to 24.62. We found an overall effect of training session on assembly salience (ANOVA-type, F2-LD-F1 model F(2,inf)=5.50, p=4.7e-03), stronger on successful prehensions compared to failed in control mice (Kruskal-Wallis, F(2,67)=8.01, p=3.0e-03), where assemblies are less salient upon re-

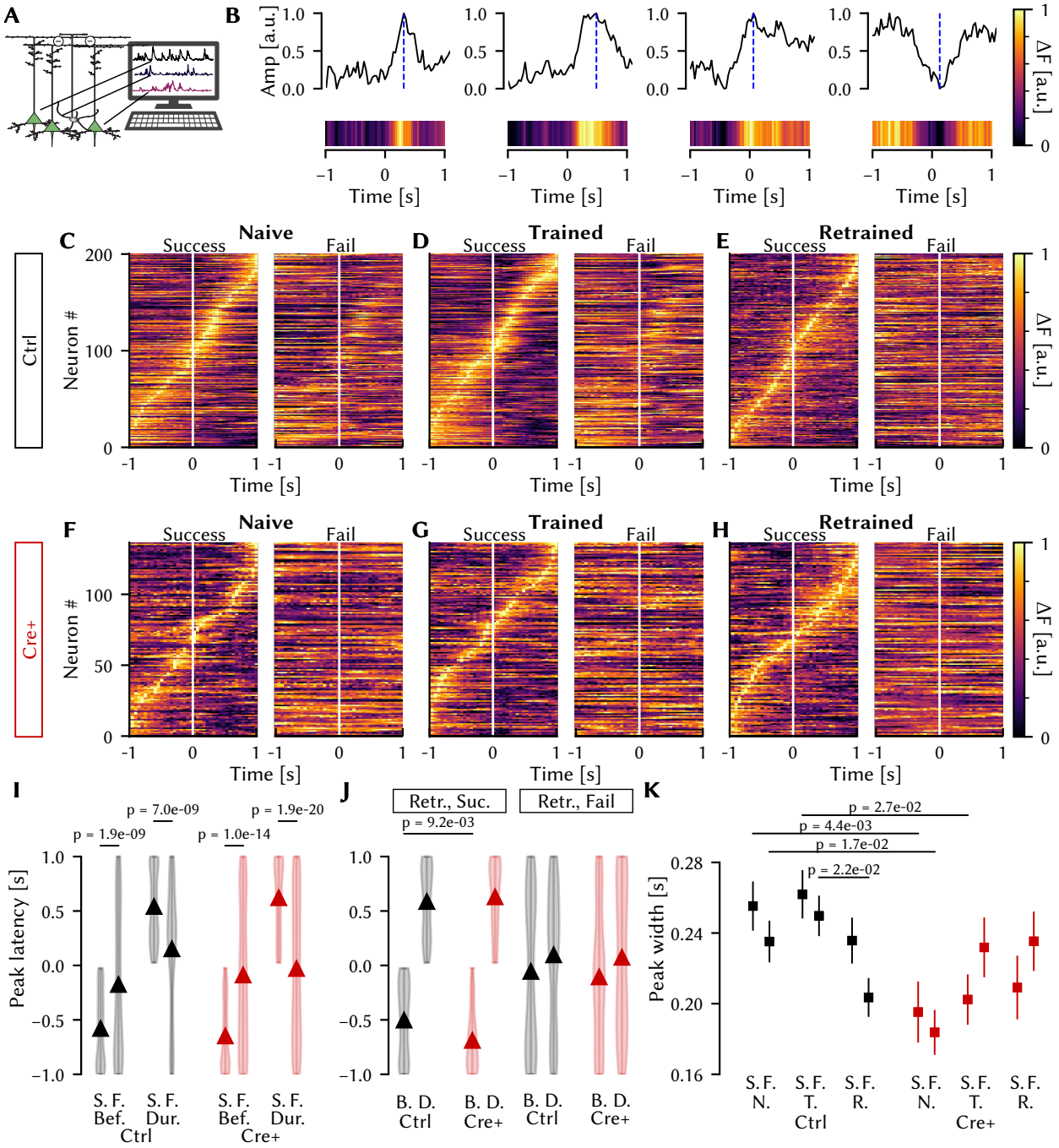

Figure 3: Distribution of PCs activity peak latencies differ between correct and incorrect prehensions. A) Schematic illustration of recorded calcium signals of GCaMP6f-expressing pyramidal cells in cortical layer 5. B) Representative examples of average fluorescence traces around prehension onset for four different neurons, showing their fluorescence curve (ΔF detr. over time) represented in a colormap, and latency of detected activity peaks (dashed blue line). C-H) Matrices (Neuron x Time x ΔF) showing normalized average fluorescence around prehension onset for each neuron, for successful (left) and failed (right) prehensions through naive, trained and retrained sessions for control (C-E) and Chrma2-Cre+ (F-H) mice. Neurons were sorted according to their temporal profile for successful prehensions, and follow the same order for failed prehensions. I) PC peak latency for successful and failed prehensions, separating neurons by the phase of their peak of activity and by genotype J) PC peak latency for prehensions on retraining, grouped by genotype and phase. K) PCs response peak width separated by genotype, session and prehension accuracy. (S., successful; F., failed; Bef., before; Dur., during prehension; N, naive; T, trained; R, retrained).

training compared to in the naive and trained sessions (Mann-Whitney U eff. sizes=0.55 and 0.42, p=3.6e-03 and 4.5e-02, respectively; Figure 4C). Also, we found an effect of genotype in naive mice (ANOVA-type, F1-LD-F1 model F(1,inf)=9.49, p = 6.2e-03), even though no punctual pairwise differences between genotypes were found.

Together, the analysis show that assembly activity is less related to the prehension movement during retraining, suggesting that the observed decrease in PC amplitude upon retraining is not general, but stronger within the prehension window; and that overexcitation of Mα2 cells during training could prevent such an effect, since no decrease in assembly salience was observed for Chrna2-Cre+ mice.

In the naive session, we identified a total of 23 assemblies in controls and 19 assemblies in Chrna2-Cre+ mice, with an average number of 5.6±0.4 cells in each assembly for each session. The number of neurons within each assembly remained fairly consistent during training and retraining (Figure 4D,E,H,I). Functional imaging studies in humans show that regional brain activity is increased and decreased during different stages of motor learning [76]. Hence, we plotted the position of the individual neurons in each assembly and measured the area which each assembly covered in the cortex. We observed an effect of genotype on the area that each assembly covered, of assemblies detected in the naive, trained and retraining sessions (Scheirer-Ray-Hare, H(1)=10.539, p=1.2e-03). Chrna2-Cre+ mice displayed a significantly smaller assembly area than control mice during retraining (n=20 control and 14 Chrna2-Cre+; Mann-Whitney U eff. size=0.495; p=1.2e-02; Figure 4F,G,J,K), suggesting that assemblies are constituted of neurons spatially closer upon Mα2 cell overexcitation during motor skill learning.

To measure PC assembly plasticity, we investigated whether assemblies detected in naive mice were preserved during and after training. The assembly resilience was calculated taking into consideration its neuronal composition, therefore reported as the percentage of neuron match, with 100% being an assembly that did not incorporate or remove any neurons over time. Although assemblies clearly change their neuronal composition with training (ANOVA-type, F1-LD-F1 model F(2,inf)= 50.43, p=1.5e-63), no effect of genotype was observed, and no difference between the trained and retraining state were observed. These results indicate that assemblies in naive mice only change their neuronal composition after the initial training session unrelated to increased Mα2 cell excitation (Figure 4L). The resilience of assemblies detected during retraining was evaluated to investigate how much the assemblies had to change neuronal composition to achieve the final configuration. In contrast to assemblies detected in naive mice, genotype and training session affected assembly resilience (ANOVA, F(2,94)=4.18, p=1.8e-02), driven by Chrna2-Cre+ mice displaying increased resilience compared to control mice (ANOVA, F(1,47)=11.325, p=2.0e-03), more strongly compared to the trained state (n=26 assemblies control and 23 assemblies Chrna2-Cre+; t-test eff. size=0.937; p=1.2e-02 Figure 4M). These results suggest that PC assemblies undergo less modifications on their neuronal composition with training when Mα2 cells are overexcited.

Ablation of Mα2 cells affected fine motor functions

In our analysis, we found robust effects from overexcited Mα2 cells on PC population and assembly plasticity in the motor cortex, however we did not observe an effect of genotype in the success ratio (Chrna2-Cre+, 6 mice; control, 8 mice; ANOVA, F(1,11)=2.43, p=0.15) when mice were administered CLZ before every session (Supplemental figure 2). To investigate if and how Mα2 cells support motor functions, we used a Caspase-based virus approach to ablate Mα2 cells in the forelimb area of the M1. After unilateral injections in Chrna2-Cre/tdTomato mice (n=2; Figure 5A) we observed a 80.4 % reduction of red fluorescent tdTomato positive cells comparing the injected to the uninjected side in the same animal (Figure 5B). In a pasta handling test, used to measure forepaw dexterity, Chrna2-Cre/tdTomato mice injected bilaterally dropped the pasta significantly more times compared with control mice (n=3 Chrna2-Cre/tdTomato, 6 controls; t-test eff. size = 1.969; p = 3.9e-02), whereas they had similar pasta handling times (Figure 5C-E). In a hanging wire test, used to evaluate parameters such as grip strength and endurance [77], the two groups of mice performed equal, both in number of falls and time spent on the wire (Figure 5F-H). In the prehension task, we did not find an interaction of genotype, although we found a significant drop in prehension performance for Chrna2-Cre/tdTomato mice, comparing the last session before ablation (n=6 mice, baseline, 599 prehensions, success ratio of 7.74%) with session 3 (after Mα2 cell ablation, 509 prehensions, success ratio of 3.68%; t-test eff. size=1.24, p=1.6e-02). No significant differences were found in control mice (n=8 mice, baseline and session 3, 989 and 743 prehensions, success ratios of 6.96 and 6.44, respectively). Thus, ablation of Mα2 cells reduced dexterity in the pasta handling task and affected prehension task success, suggesting that Mα2 cells have a role in orchestrating precise forelimb movements. However, since the tasks were performed more than a month after viral injection, the effect of Mα2 cell ablation might be partially masked by compensatory mechanisms and circuit rearrangement.

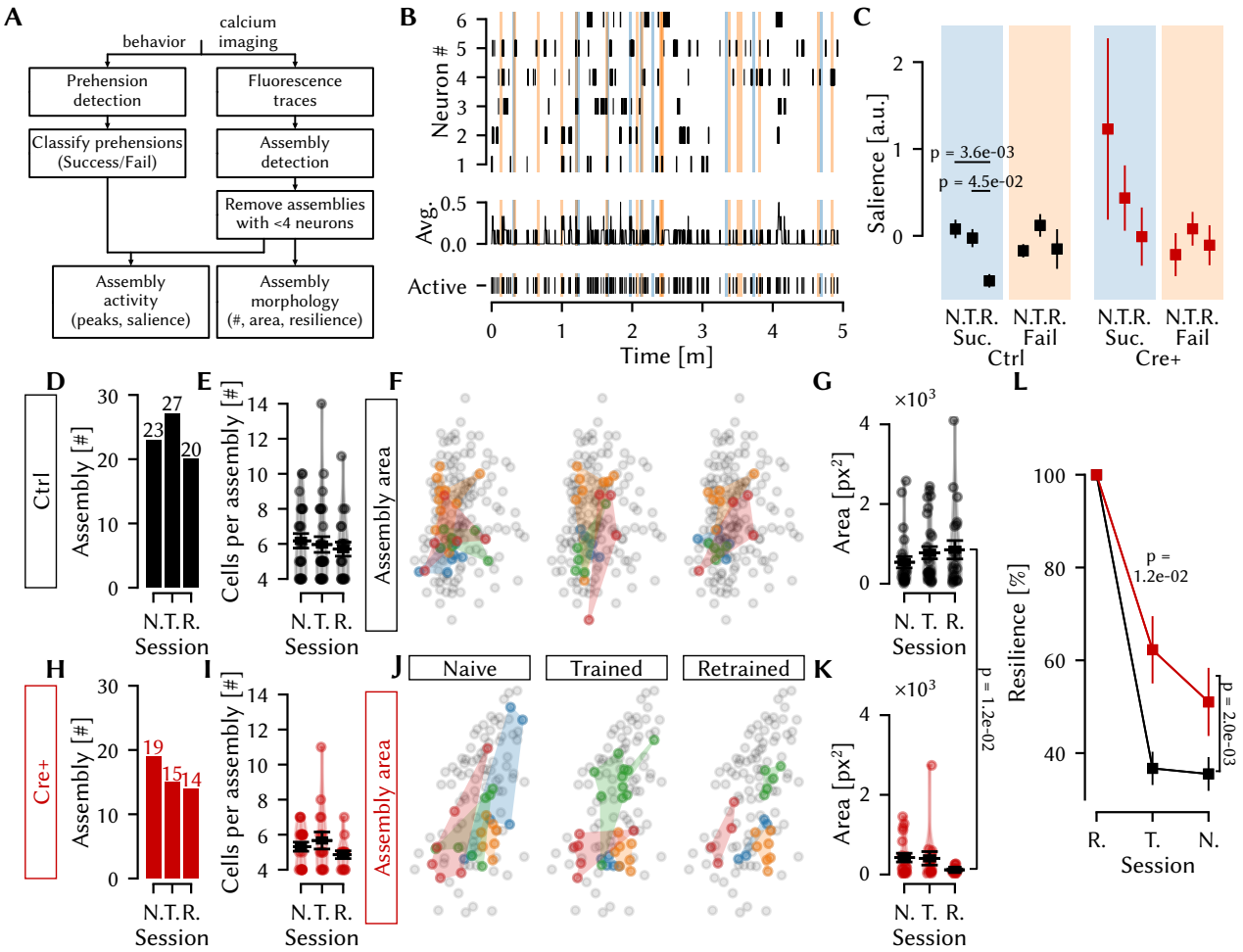

Figure 4: Mice with increased Mα2 cell excitability display assemblies with less prehension-related activity, decreased spatial area and increased resilience. A) Flowchart of the analysis pipeline. B) Activity of one representative assembly. Top, rasterized activity over the full recording time of the six neurons forming the assembly. Mid, the average of neuron activity. Bottom, the estimated rasterized activity of the assembly as a unit. Blue and orange shades show the successful and failed prehension windows, respectively. C) Salience of assemblies during the whole 2s window for each session, grouped by genotype and prehension accuracy. D-E) Number of assemblies and number of cells per assembly for control mice, detected at each session. F) Representative examples of 4 color-coded assemblies detected at session 6 and traced back to session 1. G) Area of detected assemblies at each session for control mice. H-K) Same as D-G, but for Cre+ animals. L) Resilience of assemblies for each genotype, for assemblies detected at retraining and followed back to the naive session. (Suc., successful; Fail, failed; N, naive; T, trained; R, retrained).

Increased Mα2 cell activity resulted in improved execution of a learned motor task

We reasoned that the observed reduced plasticity in PC assemblies upon Mα2 cell overexcitation, whereas not affecting motor learning efficacy, may influence already learned motor skills. Therefore, we trained mice for 7 sessions before they were injected with hDM3Gq and tested in the prehension task. For the three first subsequent sessions after viral injections, saline injections were used for a control injection response, and for three following sessions, we measured the response upon CLZ injections (Figure 6A). We found an overall effect of training session (ANOVA, F(6,54) = 4.27, p = 1.0e-03), stronger in Chrna2-Cre+ mice compared to controls (ANOVA, Chrna2-Cre+: F(6,24) = 5.612, p = 1.9e-03; Control: F(6,30) = 1.083, p = 0.395). Saline did not alter the success ratio, compared to the last training session, in any of the two groups (baseline, n=6, prehensions=512, success ratio=9.42%; control saline session 3, n=6, prehensions=974, success ratio = 13.48%, t-test, p=0.28; Chrna2-Cre+ baseline, n=5, prehensions=728, success ratio = 10.66%; Chrna2-Cre+ saline session 3, n=5, prehensions=787, success ratio=9.98%, t-test, p=0.852). In contrast, CLZ treatment resulted in a significant increase in success ratio in Chrna2-Cre+ mice compared to saline treatment (Chrna2-Cre+, saline session 3: n=5, prehensions=787, success ratio=9.98%; Chrna2-Cre+ CLZ session 3: n=5, prehensions=863, success ratio=17.7%; t-test eff. size=1.9, p=4.4e-02), which was not observed in con-

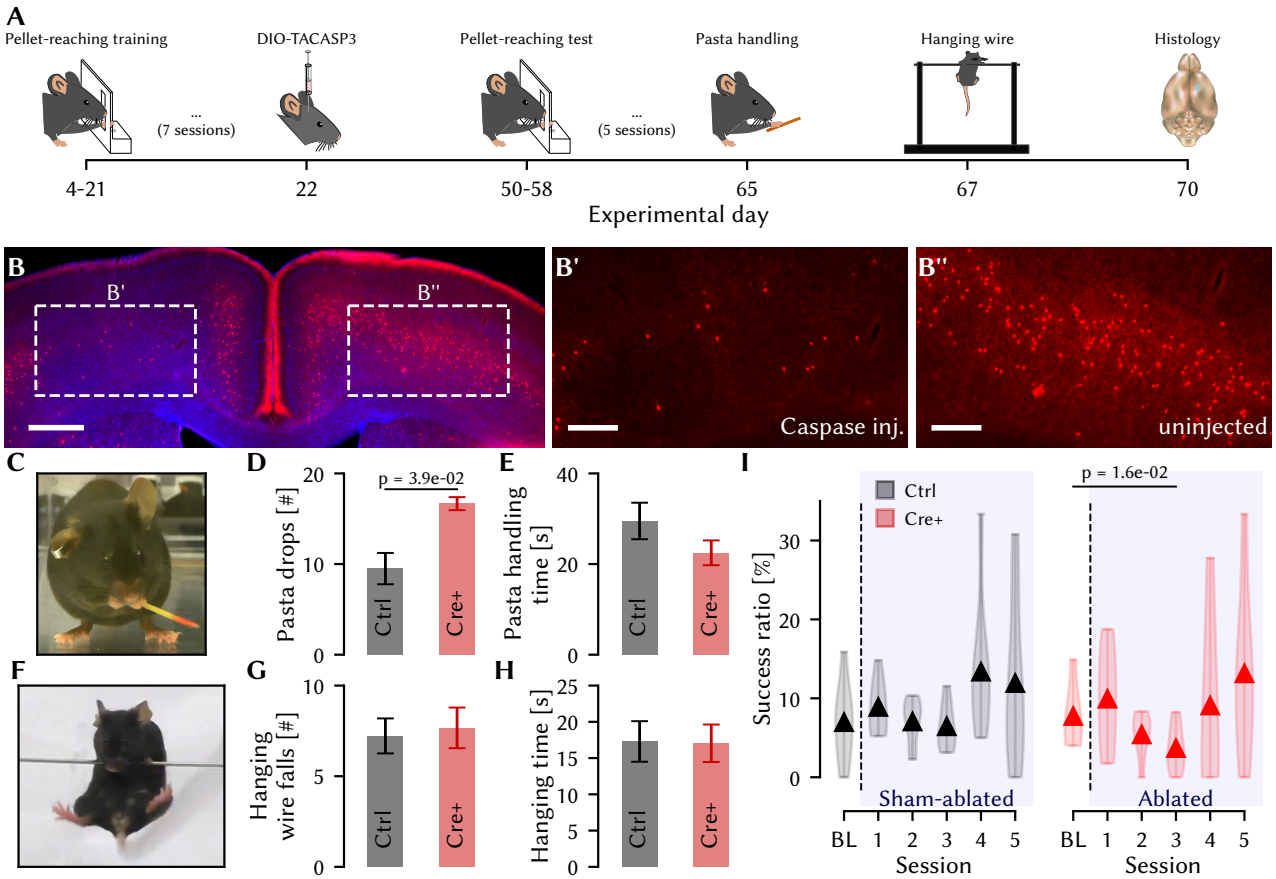

Figure 5: Apoptosis in Mα2 cells decreased pellet reaching and pasta handling performance. A) Timeline of the experiments. B) Unilateral injection of Cre-dependent TACASP3 decreased the amount of Chrna2-Cre+ cells in the motor cortex by 80.4%. Enlargement of the injected motor cortex (B'), and contralateral non-injected side (B"). Scalebars: 500μm (B) and 200μm (B' and B"). C) Animal performing the pasta handling task. D-E) Graph of results on pasta drops and time spent in the task. F) Animal performing the hanging wire task. G-H) Graph of results on falls and time spent in the task. I) Graph of results from the single pellet prehension task before and after ablation (blue shade).

trol mice (saline session 3: n=6, prehensions=974, success ratio=13.48%; CLZ session 3: n=6, prehensions=858, success ratio=14.82%; t-test eff. size = 0.009, p=0.987; Figure 6B). The mice were also implanted with electrodes for recording of local field potentials (LFP) activity. LFP activity from the last test session, in a one second window before (motor planning) and after (motor execution) in a prehension attempt was separated between successful and failed prehensions and analyzed. We found an increased LFP amplitude under CLZ treatment in Chrna2-Cre+ mice compared to control mice during successful (p=1.8e-02, Figure 6C, left), as well as failed prehensions (p=4.8e-02, Figure 6C right). Further, we found a striking difference in the LFP variance, which was strongly decreased in Chrna2-Cre+ mice compared to control mice, for both successful and failed prehensions (Levene test, p=1.3e-21; Figure 6D). Thus, chemogenetic increase of Mα2 cell activity resulted in improved execution of a learned fine motor task and significantly reduced variability of LFP amplitudes during the task.

Discussion

Here we investigated the presynaptic input to Chrna2 MCs located in layer 5 of the M1 and how these Mα2 cells impact PC population dynamics during motor learning and execution. Mα2 cells receive long-range direct inputs from the thalamic ventrolateral nucleus, substantia innominata and globus pallidus externa (Figure 7A). Further, we found that, upon increased Mα2 cell activity, parameters of plasticity at the cell, population and assembly level, all indicate decreased plasticity (Figure 7B). While increased Mα2 cell activation during training did not affect prehension accuracy, it did improve the execution of an already acquired motor skill. Thus, Mα2 cells are involved in skilled motor activities, as evidenced by altered motor performance both after loss of Mα2cells and after overexcitation of Mα2cells (Figure 7C). Our data suggest that increased Mα2cell activity reduces PC plasticity, facilitating preservation of already acquired motor skills.

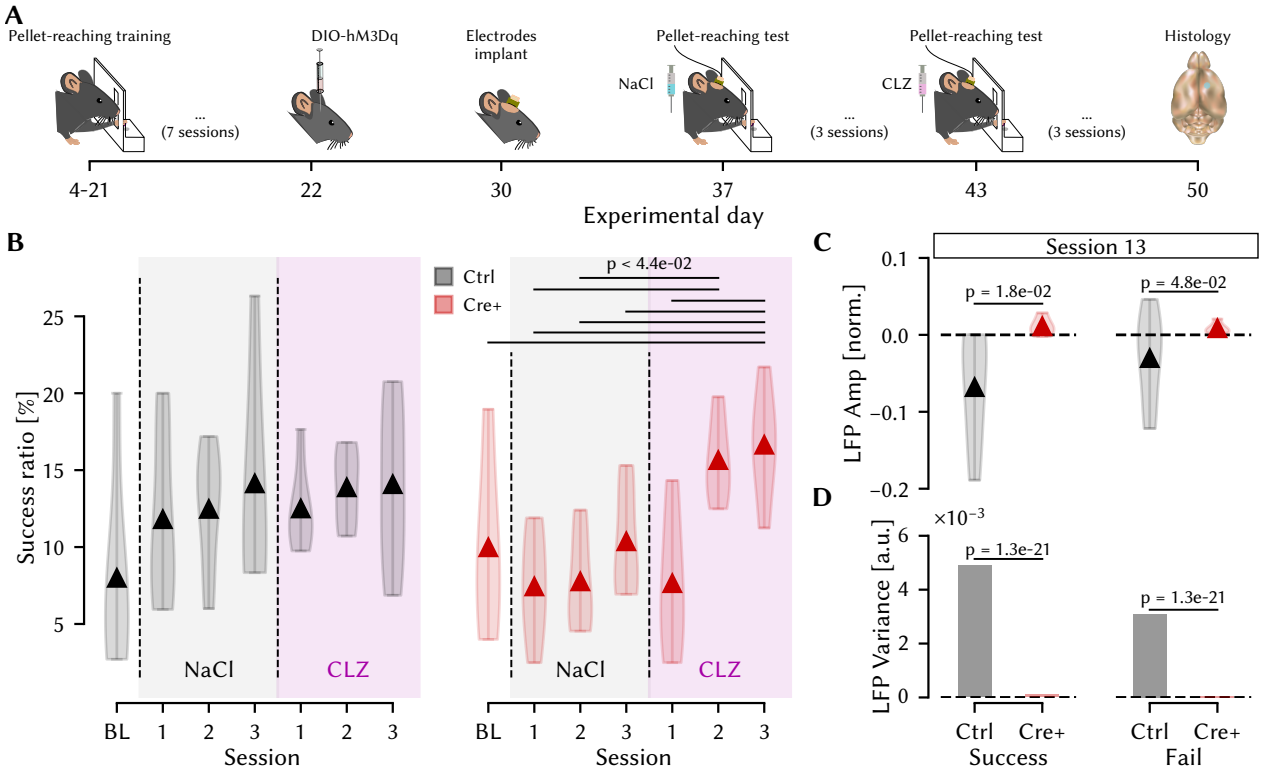

Figure 6: Mice with increased Mα2 cells excitability display increased prehension success rate, increased amplitude and decreased variance of LFP. A) Timeline of the experiments. Animals were trained to reach for the pellet and after the 7th session, the hDM3Gq was injected and the LFP electrodes implanted. B) Prehension success ratio for control (Left, black) and Chrna2-Cre+ (Right, red) mice in the sessions with saline injection (gray shade) and clozapine injection (purple shade). C) LFP mean amplitudes during prehensions for control (black) and Chrna2-Cre+(red) mice treated with clozapine for successful (left) and failed (right) trials. D) LFP variance for controls (black) and Chrna2-Cre+ (red).

Whereas a direct connection from VAL to Mα2 cells in the motor cortex has not been reported previously, VAL is the major nucleus projecting to M1 [78]. Further, neurons in the VAL are known to form monosynaptic contacts with layer 5 PCs [79] as well as to SST and PV interneurons across layer 2-6 [17]. Recent research has demonstrated that activation of high-order thalamocortical inputs can increase the activity of VIP and PV interneurons and decrease the activity of SST interneurons, resulting in disinhibition of PCs and increased synaptic plasticity [80]. The cerebellum and the basal ganglia, two key motor structures involved in tuning of movements, provide feedback signals to the cortex via the thalamus [81, 82]. The part of the motor thalamus that receives basal ganglia input projects most of its axons to layer 1 in the motor cortex, whereas the part that receives cerebellar input projects mainly to layers 3–5 [83, 84, 85, 86, 87]. Therefore, it is possible that the information being relayed from the thalamus to Mα2 cells, which have dendrites in deeper cortical layers, originates from the cerebellum (Figure 7A), the main target of proprioceptive signals important for coordinating purposeful movements [88].

During the learning process of a new motor skill, there is initially a high temporal variability of movement-related activity among PCs, but as learning progresses, a more consistent sequential activation emerges [73]. Lateral inhibition, a proposed function of inhibitory circuits in general and MCs in particular, can sharpen excitatory responses in sensory systems [89, 15]. Through inhibitory interneuron connections to adjacent excitatory PCs, it is believed that this mechanism helps establish a winner-take-all strategy, facilitating the selective excitation of the desired target. The winner-take-all concept implies that early activated PCs are more likely to silence neighboring cells, and thus become more influential "leader" PCs. It was previously shown that motor learning induces a shift in temporal activation of layer L2/3 PCs, with more PCs firing earlier post training than pre training [16]. In our PC calcium signal data, we found that robust patterns of temporal activation were strongly related to whether a prehension attempt was successful or failed, suggesting that PC temporal activation patterns are more influential than amplitudes. Specifically, the temporal profile of PCs in successful prehensions showed an early

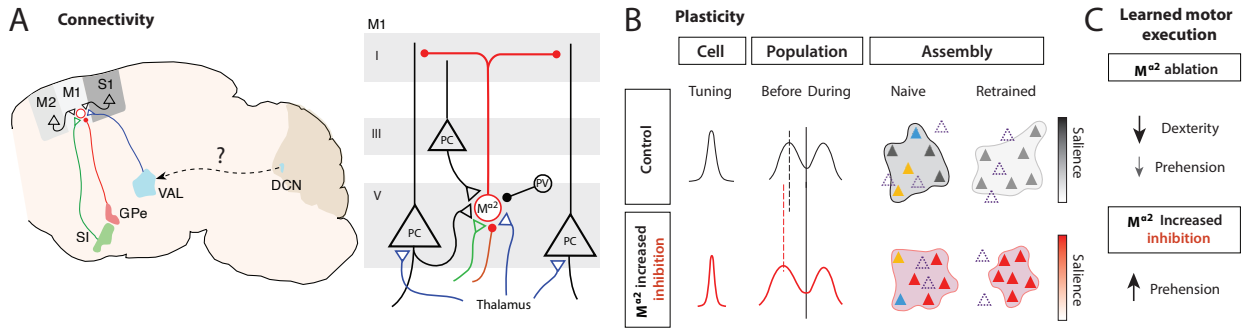

Figure 7: Summary of findings. A) Schematic illustrations of a mouse brain sagittal section and a local circuit in the primary motor cortex showing structures with monosynaptic connections to Mα2 cells in the primary motor cortex (M1). Most structures probably provide mainly excitatory input, whereas the GPe most likely provides inhibitory input (red). PCs in layer III and V project to Mα2 cells, whereas Mα2 cells project to layer V PCs. Input from cortical INs include PV positive inhibitory INs projecting to Mα2 cells. B) Schematic outline illustrating plasticity parameters. Overexcitation of Mα2 cells resulted in more narrow tuning of layer 5 PCs, a temporal shift of the average population activity in the motor planning phase, enhanced resilience, reduced physical assembly coverage and change-resistant salience upon retraining. Dashed lines mark PCs that are part of the retrained assembly but not the naive assembly, and vice versa. Blue and yellow depict PCs in the naive assembly that are part of another assembly in the retraining session. Salience values are represented by the degree of color in PCs and assembly areas. C) Mα2 cells influence fine motor movements, where caspase induced ablation of Mα2 cells resulted in decreased accuracy and dexterity, whereas overexcitation of Mα2 cells resulted in increased accuracy. M2, secondary motor cortex; S1, primary somatosensory cortex; VAL, ventral anterolateral complex of the thalamus; GPe, globus pallidus externa; SI, substantia innominata; DCN, deep cerebellar nuclei; PV, parvalbumin; MC, Mα2 cells; PC, pyramidal cell; Roman numbers refer to layer.

peak in the before prehension phase and a late peak in the during prehension phase. For failed prehensions, the PC temporal activity patterns were altered compared to successful prehensions, with a significantly later peak in the before prehension phase and an earlier peak in the during prehension phase. It has been demonstrated that SST cortical interneurons enable and maintain sequential activation of layer 2/3 PCs during motor skill learning, and that increased activity of SST interneurons is required for maintaining previously acquired layer 2/3 PC temporal activation patterns [16]. Our data, based on a more homogenous subpopulation of SST interneurons and layer 5 dynamics, showed that overexcitation of Mα2 cells resulted in altered temporal dynamics, where more PCs reached their peak activation prematurely in the motor planning phase. This was particularly apparent in relearned successful prehensions, suggesting that Mα2 cells participate in the control of layer 5 PC sequential activation for agile movements and the selection of more influential "leader" PCs during relearning events.

Hebbian learning postulates that when neurons fire synchronously, they reinforce synaptic efficiency and form an assembly. The original theory has been extended to include all cells with above-chance interactions, leading to variable definitions of neural assemblies [90]. We here adhere to the proposition that assemblies are formed by neurons that together increase their average firing rates for a specific period [91, 74], and that they can harbor varying degrees of temporal precision, scale and internal structure [92]. According to the extended theory, assemblies dynamically form, reconfigure, and fire simultaneously, with a reduced number of cells triggering the entire assembly [93]. The theory also proposes that one single neuron could participate in multiple neural assemblies, leading to distributed information coding. When PCs in our data set were sorted into assemblies, we found that the average number of cells composing the assemblies were similar regardless of Mα2 cell activation state. Notably though, the physical space of each assembly, which remained constant during learning and retraining sessions in control mice, were significantly smaller during retraining in mice with increased Mα2 cell activity, demonstrating that Mα2 cell activity can affect PC cell assembly internal structure. In learning and relearning sessions, Mα2 cell overexcitation resulted in an increased resilience in PC assemblies, suggesting that Mα2 cells contribute to PC assembly plasticity. Accordingly, during retraining, the assembly salience decreased in control mice, but not in Chrna2-Cre+ mice, further supporting that Mα2 cell overexcitation decreases plasticity and network reorganization (Figure 7B).

In the motor cortex, different motor tasks induce dendritic calcium spikes on different apical branches of individual PCs, inducing a long-lasting increase in the strength of synapses that are active at the time of spike generation. The generation of calcium spikes on different branches reduces the chance of past experiences to be disrupted by the formation of new motor programs [94]. Intriguingly, during acquisition of new skills, in mice where cell-death

was induced in SST interneurons, the maintenance of synaptic potentiation acquired during previously learned tasks was lost, which resulted in decreased performance in the initial task [94]. We found, after ablation of Mα2 cells, an increased number of drops in the pasta handling task and reduced prehension accuracy. Thus, Mα2 cells, as part of the SST population, also seem important for preserving and refining already acquired fine motor skills. Further, it has been shown that increased SST interneuron activity helps maintain previously acquired motor skills when executing a slightly different motor task, whereas decreased SST interneuron activity is important for improved motor performance and learning of the initial motor task [16, 95]. Also, the initial learning phase involves weak cortical activation of SST interneurons, and even though individual SST interneurons show diverse activity profiles during movement phases in a lever-press task, the average activity of SST interneurons increases as learning progresses [95]. We found that increased excitation of Mα2 cells during execution of a learned motor task, the single-pellet prehension task, improved the success ratio. In contrast to what has been shown for SST interneurons [16], repetitive increased activity of Mα2 cells during training did not affect motor performance. Hence, it seems that increased excitation of Mα2 cells, resulting in decreased PC assembly reconfiguration and plasticity, mainly influences the execution of already acquired motor skills and that decreased motor learning during SST interneuron activation are likely to be mediated by other SST interneuron subpopulations.

Upon Mα2 cell overexcitation, we found that LFP amplitudes became significantly less variable, indicating that Mα2 cell activation may help coordinate PC activity through synchronization. Such a reasoning is supported by previous in-vitro studies showing that Mα2 cells can synchronize PCs in a frequency-dependent manner [24]. To the contrary, SST interneuron activation has been demonstrated to cause decorrelation between neurons [96], reiterating that subpopulations of SST interneurons might have different roles in neuronal synchronization. Moreover, in our tracing effort, we identified monosynaptic cholinergic connections from the substantia innominata to Mα2 cells. Cholinergic activity is known to cause decorrelation between neurons [96], as well as to enhance cortical coding [97] and lateral inhibition via nicotinic receptor mediated depolarisation of MCs [98]. Also, cholinergic projections are highly recruited in naive untrained mice, but as motor skill learning progresses, the cholinergic recruitment decreases, resulting in increased activity of SST interneurons [95]. This begins to suggest that cholinergic modulation plays an important role in orchestrating interneuron activity and lateral inhibition during different stages of learning. It is a possibility that desynchronization of PCs is beneficial in the initial phase of learning, while synchronization of neuronal activity through Mα2 cell activation, resulting in decreased plasticity, preserves and refines already acquired motor skills.

Notably, temporal properties vary between interneuron populations and similarly, PCs are likely to be varyingly inhibited depending on the timing, synaptic weights and the position of the interneuron contact [99]. Variable tuning of circuits have been suggested to influence motor accuracy, and a proposed hypothesis postulates a central role of a local inhibitory drive [100, 101]. Accordingly, a strong inhibitory drive would decrease the directional tuning width and lead to more accurate movements, whereas reduced inhibition would lead to the opposite. Our experimental data on motor execution adhere to and support this theory, since we found that Mα2 cell ablation, i.e. less inhibition, resulted in decreased accuracy, whereas heightened excitation of Mα2 cells, i.e. more inhibition, resulted in increased accuracy and more narrow tuning of PC activity (Fig. 7B,C).

In conclusion, we have identified a role for Mα2 cells in motor control and a direct connection from cholinergic nuclei and motor related thalamic nuclei. We find that Mα2 cells are involved in temporal shaping of PC population dynamics and participate in assembly plasticity during motor learning. Further studies are warranted to address the activity patterns of Mα2 cells themselves during motor learning and whether modulation of Mα2 cell activity can affect other types of learning and skills emanating from other cortical areas.

Conflict of Interest Statement

The authors declare no conflict of interest.

Author Contributions

Methodology (AV, JW, BC, RL), Data curation (AV, JW, BC, IN, EA, KH), Validation (AV, JW, BC), Software (GN, TM), Formal analysis (AV, TM, KH, GN), Visualization (AV, BC, TM, KH, KK), Original draft preparation (KK, AV, TM, BC), Conceptualization (KK, AV, RL), Writing- Reviewing and Editing (KK, AV, TM, BC).

Funding

We thank the Swedish Foundation for International Cooperation in Research and Higher Education (STINT; www.stint.se), the Swedish Research Council (2018–02750, 2022-01245; www.vr.se) the Swedish Brain Foundation (FO2020-0228, FO2022-0018; http://hjarnfonden.se), Program for Institutional Internationalization (CAPES - PrInt, 88887.574901/2020-00), the Wenner-Gren foundations (UDP2020-0006) and Olle Engkvist Byggmästare Foundation (220-0254; https://engkviststiftelserna.se).

Acknowledgments

We thank Uppsala University behavioral facility (UUBF) and Charité for support and reagents, Juan Jiang, UmU, for establishing the prehension task.

Data Availability Statement

The datasets generated and/or analyzed in the current study are available on request.

References

[1] John F Kalaska, Stephen H Scott, Paul Cisek, and Lauren E Sergio. Cortical control of reaching movements. *Current opinion in neurobiology*, 7(6):849–859, 1997.

[2] C. E. Vargas-Irwin, G. Shakhnarovich, P. Yadollahpour, J. M. K. Mislow, M. J. Black, and J. P. Donoghue. Decoding complete reach and grasp actions from local primary motor cortex populations. *Journal of Neuroscience*, 30 (29):9659–9669, July 2010. ISSN 1529-2401. doi: 10.1523/jneurosci.5443-09.2010. URL http://dx.doi.org/10.1523/jneurosci.5443-09.2010.

[3] G.A.S Metz, V. Dietz, M.E. Schwab, and H. van de Meent. The effects of unilateral pyramidal tract section on hindlimb motor performance in the rat. *Behavioural Brain Research*, 96(1-2):37–46, 11 1998. doi: 10.1016/s0166-4328(97)00195-2. URL http://dx.doi.org/10.1016/s0166-4328(97)00195-2.

[4] RN Lemon, GW Mantel, and RB Muir. Corticospinal facilitation of hand muscles during voluntary movement in the conscious monkey. *The Journal of physiology*, 381(1): 497–527, 1986.

[5] Mengia-S Rioult-Pedotti, Daniel Friedman, and John P Donoghue. Learning-induced ltp in neocortex. *science*, 290 (5491):533–536, 2000.

[6] Tonghui Xu, Xinzhu Yu, Andrew J. Perlik, Willie F. Tobin, Jonathan A. Zweig, Kelly Tennant, Theresa Jones, and Yi Zuo. Rapid formation and selective stabilization of synapses for enduring motor memories. *Nature*, 462(7275): 915–919, November 2009. ISSN 1476-4687. doi: 10.1038/nature08389. URL http://dx.doi.org/10.1038/nature08389.

[7] Jonas A. Hosp, Ana Pekanovic, Mengia S. Rioult-Pedotti, and Andreas R. Luft. Dopaminergic projections from midbrain to primary motor cortex mediate motor skill learning. *The Journal of Neuroscience*, 31(7):2481–2487, February 2011. ISSN 1529-2401. doi: 10.1523/jneurosci.5411-10.2011. URL http://dx.doi.org/10.1523/jneurosci.5411-10.2011.

[8] Risa Kawai, Timothy Markman, Rajesh Poddar, Raymond Ko, Antoniu L. Fantana, Ashesh K. Dhawale, Adam R. Kampff, and Bence P. Ölveczky. Motor cortex is required for learning but not for executing a motor skill. *Neuron*, 86(3):800–812, May 2015. ISSN 0896-6273. doi: 10.1016/j.neuron.2015.03.024. URL http://dx.doi.org/10.1016/j.neuron.2015.03.024.

[9] Jian-Zhong Guo, Austin R Graves, Wendy W Guo, Jihong Zheng, Allen Lee, Juan Rodríguez-González, Nuo Li, John J Macklin, James W Phillips, Brett D Mensh, et al. Cortex commands the performance of skilled movement. *Elife*, 4: e10774, 2015.

[10] Henry Markram, Maria Toledo-Rodriguez, Yun Wang, Anirudh Gupta, Gilad Silberberg, and Caizhi Wu. Interneurons of the neocortical inhibitory system. *Nature Reviews Neuroscience*, 5(10):793–807, October 2004. ISSN 1471-0048. doi: 10.1038/nrn1519. URL http://dx.doi.org/10.1038/nrn1519.

[11] Jesse H. Goldberg, Clay O. Lacefield, and Rafael Yuste. Global dendritic calcium spikes in mouse layer 5 low threshold spiking interneurones: implications for control of pyramidal cell bursting. *The Journal of Physiology*, 558(2): 465–478, July 2004. ISSN 1469-7793. doi: 10.1113/jphysiol.2004.064519. URL http://dx.doi.org/10.1113/jphysiol.2004.064519.

[12] Masanori Murayama, Enrique Pérez-Garci, Thomas Nevian, Tobias Bock, Walter Senn, and Matthew E. Larkum. Dendritic encoding of sensory stimuli controlled by deep cortical interneurons. *Nature*, 457(7233):1137–1141, January 2009. ISSN 1476-4687. doi: 10.1038/nature07663. URL http://dx.doi.org/10.1038/nature07663.

[13] James Kozloski, Farid Hamzei-Sichani, and Rafael Yuste. Stereotyped position of local synaptic targets in neocortex. *Science*, 293(5531):868–872, 2001.

[14] Christoph Kapfer, Lindsey L Glickfeld, Bassam V Atallah, and Massimo Scanziani. Supralinear increase of recurrent inhibition during sparse activity in the somatosensory cortex. *Nature Neuroscience*, 10(6):743–753, May 2007. ISSN 1546-1726. doi: 10.1038/nn1909. URL http://dx.doi.org/10.1038/nn1909.

[15] Gilad Silberberg and Henry Markram. Disynaptic inhibition between neocortical pyramidal cells mediated by martinotti cells. *Neuron*, 53(5):735–746, March 2007. ISSN 0896-6273. doi: 10.1016/j.neuron.2007.02.012. URL http://dx.doi.org/10.1016/j.neuron.2007.02.012.

[16] Avital Adler, Ruohe Zhao, Myung Eun Shin, Ryohei Yasuda, and Wen-Biao Gan. Somatostatin-expressing interneurons enable and maintain learning-dependent sequential activation of pyramidal neurons. *Neuron*, 102(1):202–216.e7, April 2019. ISSN 0896-6273. doi: 10.1016/j.neuron.2019.01.036. URL http://dx.doi.org/10.1016/j.neuron.2019.01.036.

[17] Sandra U. Okoro, Roman U. Goz, Brigdet W. Njeri, Madhumita Harish, Catherine F. Ruff, Sarah E. Ross, Charles Gerfen, and Bryan M. Hooks. Organization of cortical and thalamic input to inhibitory neurons in mouse motor cortex. *The Journal of Neuroscience*, 42(43):8095–8112, September 2022. ISSN 1529-2401. doi: 10.1523/jneurosci.0950-22.2022. URL http://dx.doi.org/10.1523/jneurosci.0950-22.2022.

[18] William Muñoz, Robin Tremblay, Daniel Levenstein, and Bernardo Rudy. Layer-specific modulation of neocortical dendritic inhibition during active wakefulness. *Science*, 355 (6328):954–959, 2017.

[19] Therese Riedemann. Diversity and function of somatostatin-expressing interneurons in the cerebral cortex. *International Journal of Molecular Sciences*, 20(12):2952, June 2019. ISSN 1422-0067. doi: 10.3390/ijms20122952. URL http://dx.doi.org/10.3390/ijms20122952.

[20] McGarry. Quantitative classification of somatostatin-positive neocortical interneurons identifies three interneuron subtypes. *Frontiers in Neural Circuits*, 2010. ISSN 1662-5110. doi: 10.3389/fncir.2010.00012. URL http://dx.doi.org/10.3389/fncir.2010.00012.

[21] Yun Wang, Maria Toledo-Rodriguez, Anirudh Gupta, Caizhi Wu, Gilad Silberberg, Junyi Luo, and Henry Markram. Anatomical, physiological and molecular properties of martinotti cells in the somatosensory cortex of the juvenile rat. *The Journal of Physiology*, 561(1):65–90, November 2004. ISSN 1469-7793. doi: 10.1113/jphysiol.2004.073353. URL http://dx.doi.org/10.1113/jphysiol.2004.073353.

[22] Nathan W Gouwens, Staci A Sorensen, Fahimeh Baftizadeh, Agata Budzillo, Brian R Lee, Tim Jarsky, Lauren Alfiler, Katherine Baker, Eliza Barkan, Kyla Berry, et al. Integrated morphoelectric and transcriptomic classification of cortical gabaergic cells. *Cell*, 183(4):935–953.e19, November 2020. ISSN 0092-8674. doi: 10.1016/j.cell.2020.09.057. URL http://dx.doi.org/10.1016/j.cell.2020.09.057.

[23] Sherry Jingjing Wu, Elaine Sevier, Deepanjali Dwivedi, Giuseppe-Antonio Saldi, Ariel Hairston, Sabrina Yu, Lydia Abbott, Da Hae Choi, Mia Sherer, Yanjie Qiu, Ashwini Shinde, Mackenzie Lenahan, Daniella Rizzo, Qing Xu, Irving Barrera, Vipin Kumar, Giovanni Marrero, Alvar Prönneke, Shuhan Huang, Klas Kullander, David A. Stafford, Evan Macosko, Fei Chen, Bernardo Rudy, and Gord Fishell. Cortical somatostatin interneuron subtypes form cell-type-specific circuits. *Neuron*, 111(17):2675–2692.e9, September 2023. ISSN 0896-6273. doi: 10.1016/j.neuron.2023.05.032. URL http://dx.doi.org/10.1016/j.neuron.2023.05.032.

[24] Markus M. Hilscher, Richardson N. Leão, Steven J. Edwards, Katarina E. Leão, and Klas Kullander. Chrna2-martinotti cells synchronize layer 5 type a pyramidal cells via rebound excitation. *PLOS Biology*, 15(2):e2001392, February 2017. ISSN 1545-7885. doi: 10.1371/journal.pbio.2001392. URL http://dx.doi.org/10.1371/journal.pbio.2001392.

[25] Richardson N Leão, Sanja Mikulovic, Katarina E Leão, Hermany Munguba, Henrik Gezelius, Anders Enjin, Kalicharan Patra, Anders Eriksson, Leslie M Loew, Adriano B L Tort, and Klas Kullander. Olm interneurons differentially modulate ca3 and entorhinal inputs to hippocampal ca1 neurons. *Nature Neuroscience*, 15(11):1524–1530, October 2012. ISSN 1546-1726. doi: 10.1038/nn.3235. URL http://dx.doi.org/10.1038/nn.3235.

[26] Linda Madisen, Theresa A Zwingman, Susan M Sunkin, Seung Wook Oh, Hatim A Zariwala, Hong Gu, Lydia L Ng, Richard D Palmiter, Michael J Hawrylycz, Allan R Jones, et al. A robust and high-throughput cre reporting and characterization system for the whole mouse brain. *Nature neuroscience*, 13(1):133–140, 2010.

[27] Vitor H. Sousa, Goichi Miyoshi, Jens Hjerling-Leffler, Theofanis Karayannis, and Gord Fishell. Characterization of nkx6-2-derived neocortical interneuron lineages. *Cerebral Cortex*, 19 (1):i1–i10, April 2009. ISSN 1047-3211. doi: 10.1093/cercor/bhp038. URL http://dx.doi.org/10.1093/cercor/bhp038.

[28] George Paxinos and Keith BJ Franklin. *Paxinos and Franklin's the mouse brain in stereotaxic coordinates*. Academic press, 2019.

[29] Xuhua Wang, Yuanyuan Liu, Xinjian Li, Zicong Zhang, Hengfu Yang, Yu Zhang, Philip R. Williams, Noaf S.A. Alwahab, Kush Kapur, Bin Yu, Yiming Zhang, Mengying Chen, Haixia Ding, Charles R. Gerfen, Kuan Hong Wang, and Zhigang He. Deconstruction of corticospinal circuits for goal-directed motor skills. *Cell*, 171(2):440–455.e14, October 2017. ISSN 0092-8674. doi: 10.1016/j.cell.2017.08.014. URL http://dx.doi.org/10.1016/j.cell.2017.08.014.

[30] Kelly A. Tennant, Aaron L. Asay, Rachel P. Allred, Angela R. Ozburn, Jeffrey A. Kleim, and Theresa A. Jones. The vermicelli and capellini handling tests: Simple quantitative measures of dexterous forepaw function in rats and mice. *Journal of Visualized Experiments*, (41), July 2010. ISSN 1940-087X. doi: 10.3791/2076. URL http://dx.doi.org/10.3791/2076.

[31] Kazunari Miyamichi, Yael Shlomai-Fuchs, Marvin Shu, Brandon C Weissbourd, Liqun Luo, and Adi Mizrahi. Dissecting local circuits: parvalbumin interneurons underlie broad feedback control of olfactory bulb output. *Neuron*, 80(5): 1232–1245, 2013.

[32] Juan L. Gomez, Jordi Bonaventura, Wojciech Lesniak, William B. Mathews, Polina Sysa-Shah, Lionel A. Rodriguez, Randall J. Ellis, Christopher T. Richie, Brandon K. Harvey, Robert F. Dannals, Martin G. Pomper, Antonello Bonci, and Michael Michaelides. Chemogenetics revealed: Dreadd occupancy and activation via converted clozapine. *Science*, 357(6350):503â€“507, August 2017. ISSN 1095-9203. doi: 10.1126/science.aan2475. URL http://dx.doi.org/10.1126/science.aan2475.

[33] Daniel F. Manvich, Kevin A. Webster, Stephanie L. Foster, Martilias S. Farrell, James C. Ritchie, Joseph H. Porter, and David Weinshenker. The dreadd agonist clozapine n-oxide (cno) is reverse-metabolized to clozapine and produces clozapine-like interoceptive stimulus effects in rats and mice. *Scientific Reports*, 8(1), March 2018. ISSN 2045-2322. doi: 10.1038/s41598-018-22116-z. URL http://dx.doi.org/10.1038/s41598-018-22116-z.

[34] Lewis Couchman, Phillip Edgar Morgan, Edgar Pathrose Spencer, and Robert James Flanagan. Plasma clozapine, norclozapine, and the clozapine: norclozapine ratio in relation to prescribed dose and other factors: data from a therapeutic drug monitoring service, 1993–2007. *Therapeutic drug monitoring*, 32(4):438–447, 2010. doi: 10.1097/FTD.0b013e3181dad1fb. URL http://dx.doi.org/10.1097/FTD.0b013e3181dad1fb.

[35] Pengcheng Zhou, Shanna L Resendez, Jose Rodriguez-Romaguera, Jessica C Jimenez, Shay Q Neufeld, Andrea Giovannucci, Johannes Friedrich, Eftychios A Pnevmatikakis, Garret D Stuber, Rene Hen, Mazen A Kheirbek, Bernardo L Sabatini, Robert E Kass, and Liam Paninski. Efficient and accurate extraction of in vivo calcium signals from microendoscopic video data. *eLife*, 7, February 2018. ISSN 2050-084X. doi: 10.7554/elife.28728. URL http://dx.doi.org/10.7554/elife.28728.

[36] Andrea Giovannucci, Johannes Friedrich, Pat Gunn, Jérémie Kalfon, Brandon L Brown, Sue Ann Koay, Jiannis Taxidis, Farzaneh Najafi, Jeffrey L Gauthier, Pengcheng Zhou, et al. Caiman an open source tool for scalable calcium imaging data analysis. *elife*, 8:e38173, 2019. doi: 10.7554/elife.38173.001.

[37] Jan Mölter, Lilach Avitan, and Geoffrey J. Goodhill. Detecting neural assemblies in calcium imaging data. *BMC Biology*, 16(1), nov 2018. doi: 10.1186/s12915-018-0606-4. URL https://doi.org/10.1186/s12915-018-0606-4.

[38] Johannes Schindelin, Ignacio Arganda-Carreras, Erwin Frise, Verena Kaynig, Mark Longair, Tobias Pietzsch, Stephan Preibisch, Curtis Rueden, Stephan Saalfeld, Benjamin Schmid, Jean-Yves Tinevez, Daniel James White, Volker Hartenstein, Kevin Eliceiri, Pavel Tomancak, and Albert Cardona. Fiji: an open-source platform for biological-image analysis. *Nature Methods*, 9(7):676–682, June 2012. ISSN 1548-7105. doi: 10.1038/nmeth.2019. URL http://dx.doi.org/10.1038/nmeth.2019.

[39] Kimihiro Noguchi, Yulia R. Gel, Edgar Brunner, and Frank Konietschke. ¡b¿nparld¡/b¿: An¡i¿r¡/i¿software package for the nonparametric analysis of longitudinal data in factorial experiments. *Journal of Statistical Software*, 50(12), 2012. doi: 10.18637/jss.v050.i12. URL http://dx.doi.org/10.18637/jss.v050.i12.

[40] Richard L Gorsuch and Curtis Lehmann. Chi-square and f ratio: Which should be used when? *Journal of Methods and Measurement in the Social Sciences*, 8(2):58–71, 2017.

[41] Joshua H Siegle, Gregory J Hale, Jonathan P Newman, and Jakob Voigts. Neural ensemble communities: open-source approaches to hardware for large-scale electrophysiology. *Current Opinion in Neurobiology*, 32:53–59, jun 2015. doi: 10.1016/j.conb.2014.11.004. URL https://doi.org/10.1016/j.conb.2014.11.004.

[42] Pauli Virtanen, Ralf Gommers, Travis E. Oliphant, Matt Haberland, Tyler Reddy, David Cournapeau, Evgeni Burovski, Pearu Peterson, Warren Weckesser, Jonathan Bright, Stéfan J. van der Walt, Matthew Brett, Joshua Wilson, K. Jarrod Millman, Nikolay Mayorov, Andrew R. J. Nelson, Eric Jones, Robert Kern, Eric Larson, C J Carey, Ilhan Polat, Yu Feng, Eric W. Moore, Jake VanderPlas, Denis Laxalde, Josef Perktold, Robert Cimrman, Ian Henriksen, E. A. Quintero, Charles R. Harris, Anne M. Archibald, Antônio H. Ribeiro, Fabian Pedregosa, Paul van Mulbregt, and SciPy 1.0 Contributors. SciPy 1.0: Fundamental Algorithms for Scientific Computing in Python. *Nature Methods*, 17:261–272, 2020. doi: 10.1038/s41592-019-0686-2.

[43] Charles R. Harris, K. Jarrod Millman, Stéfan J van der Walt, Ralf Gommers, Pauli Virtanen, David Cournapeau, Eric Wieser, Julian Taylor, Sebastian Berg, Nathaniel J. Smith, Robert Kern, Matti Picus, Stephan Hoyer, Marten H. van Kerkwijk, Matthew Brett, Allan Haldane, Jaime Fernández del Río, Mark Wiebe, Pearu Peterson, Pierre Gérard-Marchant, Kevin Sheppard, Tyler Reddy, Warren Weckesser, Hameer Abbasi, Christoph Gohlke, and Travis E. Oliphant. Array programming with NumPy. *Nature*, 585: 357–362, 2020. doi: 10.1038/s41586-020-2649-2.

[44] Thawann Malfatti and Barbara Ciralli. Sciscripts, 2023. URL https://zenodo.org/record/4045872. Software.

[45] John D. Hunter. Matplotlib: A 2d Graphics Environment. *Computing in Science & Engineering*, 9(3):90–95, 2007. ISSN 1521-9615. doi: 10.1109/MCSE.2007.55. URL http://ieeexplore.ieee.org/document/4160265/.

[46] Inkscape Project. Inkscape, 2022. URL https://inkscape.org. Software.

[47] G. Bradski. The OpenCV Library. *Dr. Dobb's Journal of Software Tools*, 2000.

[48] Tanmay Nath, Alexander Mathis, An Chi Chen, Amir Patel, Matthias Bethge, and Mackenzie Weygandt Mathis. Using deeplabcut for 3d markerless pose estimation across species and behaviors. *Nature protocols*, 14(7):2152–2176, jun 2019. doi: 10.1038/s41596-019-0176-0. URL https://doi.org/10.1038/s41596-019-0176-0.

[49] Ian R. Wickersham, David C. Lyon, Richard J.O. Barnard, Takuma Mori, Stefan Finke, Karl-Klaus Conzelmann, John A.T. Young, and Edward M. Callaway. Monosynaptic restriction of transsynaptic tracing from single, genetically targeted neurons. *Neuron*, 53(5):639–647, March 2007. ISSN 0896-6273. doi: 10.1016/j.neuron.2007.01.033. URL http://dx.doi.org/10.1016/j.neuron.2007.01.033.

[50] Nadin Hagendorf and Karl-Klaus Conzelmann. Recovery of replication-competent and g-gene-deleted rabies viruses from cdna. *Cold Spring Harbor Protocols*, 2015(12): pdb.prot089409, December 2015. ISSN 1559-6095. doi: 10.1101/pdb.prot089409. URL http://dx.doi.org/10.1101/pdb.prot089409.

[51] Anna Velica and Klas Kullander. A flowchart for adequate controls in virus-based monosynaptic tracing experiments identified cre-independent leakage of the tva receptor in rϕgt mice. *BMC neuroscience*, 25(1):1–9, 2024.

[52] David W Franklin and Daniel M Wolpert. Computational mechanisms of sensorimotor control. *Neuron*, 72(3):425–442, 2011.

[53] Bernardo Rudy, Gordon Fishell, SooHyun Lee, and Jens Hjerling-Leffler. Three groups of interneurons account for nearly 100gabaergic neurons. *Developmental Neurobiology*, 71(1):45–61, December 2010. ISSN 1932-846X. doi: 10.1002/dneu.20853. URL http://dx.doi.org/10.1002/dneu.20853.

[54] Robin Tremblay, Soohyun Lee, and Bernardo Rudy. Gabaergic interneurons in the neocortex: From cellular properties to circuits. *Neuron*, 91(2):260–292, July 2016. ISSN 0896-6273. doi: 10.1016/j.neuron.2016.06.033. URL http://dx.doi.org/10.1016/j.neuron.2016.06.033.

[55] Carsten K Pfeffer, Mingshan Xue, Miao He, Z Josh Huang, and Massimo Scanziani. Inhibition of inhibition in visual cortex: the logic of connections between molecularly distinct interneurons. *Nature Neuroscience*, 16(8):1068–1076, June 2013. ISSN 1546-1726. doi: 10.1038/nn.3446. URL http://dx.doi.org/10.1038/nn.3446.

[56] F. Walker, M. MÃ¶ck, M. Feyerabend, J. Guy, R. J. Wagener, D. Schubert, J. F. Staiger, and M. Witte. Parvalbumin- and vasoactive intestinal polypeptide-expressing neocortical interneurons impose differential inhibition on martinotti cells. *Nature Communications*, 7(1), November 2016. ISSN 2041-1723. doi: 10.1038/ncomms13664. URL http://dx.doi.org/10.1038/ncomms13664.

[57] Han Xu, Hyo-Young Jeong, Robin Tremblay, and Bernardo Rudy. Neocortical somatostatin-expressing gabaergic interneurons disinhibit the thalamorecipient layer 4. *Neuron*, 77(1):155–167, January 2013. ISSN 0896-6273. doi: 10.1016/j.neuron.2012.11.004. URL http://dx.doi.org/10.1016/j.neuron.2012.11.004.

[58] Arpiar Saunders, Ian A. Oldenburg, Vladimir K. Berezovskii, Caroline A. Johnson, Nathan D. Kingery, Hunter L. Elliott, Tiao Xie, Charles R. Gerfen, and Bernardo L. Sabatini. A direct gabaergic output from the basal ganglia to frontal cortex. *Nature*, 521(7550):85â€“89, March 2015. ISSN 1476-4687. doi: 10.1038/nature14179. URL http://dx.doi.org/10.1038/nature14179.

[59] Jie Dong, Sarah Hawes, Junbing Wu, Weidong Le, and Huaibin Cai. Connectivity and functionality of the globus pallidus externa under normal conditions and parkinsonâ€™s disease. *Frontiers in Neural Circuits*, 15, March 2021. ISSN 1662-5110. doi: 10.3389/fncir.2021.645287. URL http://dx.doi.org/10.3389/fncir.2021.645287.

[60] Zhong S. Zheng and Martin M. Monti. Cortical and thalamic connections of the human globus pallidus: Implications for disorders of consciousness. *Frontiers in Neuroanatomy*, 16, August 2022. ISSN 1662-5129. doi: 10.3389/fnana.2022.960439. URL http://dx.doi.org/10.3389/fnana.2022.960439.

[61] Ingvild E. Bjerke, Sharon C. Yates, Arthur Laja, Menno P. Witter, Maja A. Puchades, Jan G. Bjaalie, and Trygve B. Leergaard. Densities and numbers of calbindin and parvalbumin positive neurons across the rat and mouse brain. *iScience*, 24(1):101906, 1 2021. doi: 10.1016/j.isci.2020.101906. URL http://dx.doi.org/10.1016/j.isci.2020.101906.

[62] Jerome N Sanes and John P Donoghue. Plasticity and primary motor cortex. *Annual review of neuroscience*, 23(1): 393–415, 2000.

[63] Blaine N. Armbruster, Xiang Li, Mark H. Pausch, Stefan Herlitze, and Bryan L. Roth. Evolving the lock to fit the key to create a family of g protein-coupled receptors potently activated by an inert ligand. *Proceedings of the National Academy of Sciences*, 104(12):5163–5168, 3 2007. doi: 10.1073/pnas.0700293104. URL http://dx.doi.org/10.1073/pnas.0700293104.

[64] Cornelis van de Kamp and Frank T. J. M. Zaal. Prehension is really reaching and grasping. *Experimental Brain Research*, 182(1):27–34, May 2007. ISSN 1432-1106. doi: 10.1007/s00221-007-0968-2. URL http://dx.doi.org/10.1007/s00221-007-0968-2.

[65] Chia-Chien Chen, Anthony Gilmore, and Yi Zuo. Study motor skill learning by single-pellet reaching tasks in mice. *JoVE (Journal of Visualized Experiments)*, (85):e51238, 2014.

[66] Eiman Azim, Juan Jiang, Bror Alstermark, and Thomas M. Jessell. Skilled reaching relies on a v2a propriospinal internal copy circuit. *Nature*, 508(7496):357–363, February 2014. ISSN 1476-4687. doi: 10.1038/nature13021. URL http://dx.doi.org/10.1038/nature13021.

[67] Eddy Albarran, Aram Raissi, Omar Jáidar, Carla J. Shatz, and Jun B. Ding. Enhancing motor learning by increasing the stability of newly formed dendritic spines in the motor cortex. 109(20):3298–3311.e4, oct 2021. doi: 10.1016/j.neuron.2021.07.030. URL https://doi.org/10.1016/j.neuron.2021.07.030.

[68] Tsai-Wen Chen, Trevor J. Wardill, Yi Sun, Stefan R. Pulver, Sabine L. Renninger, Amy Baohan, Eric R. Schreiter, Rex A. Kerr, Michael B. Orger, Vivek Jayaraman, Loren L. Looger, Karel Svoboda, and Douglas S. Kim. Ultrasensitive fluorescent proteins for imaging neuronal activity. *Nature*, 499 (7458):295–300, July 2013. ISSN 1476-4687. doi: 10.1038/nature12354. URL http://dx.doi.org/10.1038/nature12354.

[69] Junichi Nakai, Masamichi Ohkura, and Keiji Imoto. A high signal-to-noise ca2+ probe composed of a single green fluorescent protein. *Nature Biotechnology*, 19(2):137–141, 2 2001. doi: 10.1038/84397. URL http://dx.doi.org/10.1038/84397.

[70] Atsushi Miyawaki, Juan Llopis, Roger Heim, J Michael McCaffery, Joseph A Adams, Mitsuhiko Ikura, and Roger Y Tsien. Fluorescent indicators for ca2+ based on green fluorescent proteins and calmodulin. *Nature*, 388(6645):882–887, 1997.

[71] Juergen C. Jung, Amit D. Mehta, Emre Aksay, Raymond Stepnoski, and Mark J. Schnitzer. In vivo mammalian brain imaging using one- and two-photon fluorescence microendoscopy. *Journal of Neurophysiology*, 92(5):3121–3133, November 2004. ISSN 1522-1598. doi: 10.1152/jn.00234.2004. URL http://dx.doi.org/10.1152/jn.00234.2004.

[72] Shanna L Resendez, Josh H Jennings, Randall L Ung, Vijay Mohan K Namboodiri, Zhe Charles Zhou, James M Otis, Hiroshi Nomura, Jenna A McHenry, Oksana Kosyk, and Garret D Stuber. Visualization of cortical, subcortical and deep brain neural circuit dynamics during naturalistic mammalian behavior with head-mounted microscopes and chronically implanted lenses. *Nature Protocols*, 11(3):566–597, February 2016. ISSN 1750-2799. doi: 10.1038/nprot.2016.021. URL http://dx.doi.org/10.1038/nprot.2016.021.

[73] Andrew J. Peters, Simon X. Chen, and Takaki Komiyama. Emergence of reproducible spatiotemporal activity during motor learning. *Nature*, 510(7504):263–267, May 2014. ISSN 1476-4687. doi: 10.1038/nature13235. URL http://dx.doi.org/10.1038/nature13235.

[74] Vítor Lopes-dos Santos, Sidarta Ribeiro, and Adriano B.L. Tort. Detecting cell assemblies in large neuronal populations. *Journal of Neuroscience Methods*, 220(2):149–166, November 2013. ISSN 0165-0270. doi: 10.1016/j.jneumeth.2013.04.010. URL http://dx.doi.org/10.1016/j.jneumeth.2013.04.010.

[75] Jeremy S. Biane, Yoshio Takashima, Massimo Scanziani, James M. Conner, and Mark H. Tuszynski. Reorganization of recurrent layer 5 corticospinal networks following adult motor training. *The Journal of Neuroscience*, 39 (24):4684–4693, April 2019. ISSN 1529-2401. doi: 10.1523/jneurosci.3442-17.2019. URL http://dx.doi.org/10.1523/jneurosci.3442-17.2019.

[76] A. Floyer-Lea and P. M. Matthews. Distinguishable brain activation networks for short- and long-term motor skill learning. *Journal of Neurophysiology*, 94(1):512–518, July 2005. ISSN 1522-1598. doi: 10.1152/jn.00717.2004. URL http://dx.doi.org/10.1152/jn.00717.2004.

[77] Jingsong Ruan and Yao Yao. Behavioral tests in rodent models of stroke. *Brain Hemorrhages*, 1(4):171–184, December 2020. ISSN 2589-238X. doi: 10.1016/j.hest.2020.09.001. URL http://dx.doi.org/10.1016/j.hest.2020.09.001.

[78] Toshio Terashima, Kaoru Inoue, Yoshiro Inoue, and Katsuhiko Mikoshiba. Thalamic connectivity of the primary motor cortex of normal and reeler mutant mice. *Journal of Comparative Neurology*, 257(3):405–421, 1987.

[79] Bryan M. Hooks, Tianyi Mao, Diego A. Gutnisky, Naoki Yamawaki, Karel Svoboda, and Gordon M. G. Shepherd. Organization of cortical and thalamic input to pyramidal neurons in mouse motor cortex. *The Journal of Neuroscience*, 33(2):748–760, January 2013. ISSN 1529-2401. doi: 10.1523/jneurosci.4338-12.2013. URL http://dx.doi.org/10.1523/jneurosci.4338-12.2013.

[80] Leena E. Williams and Anthony Holtmaat. Higher-order thalamocortical inputs gate synaptic long-term potentiation via disinhibition. *Neuron*, 101(1):91–102.e4, January 2019. ISSN 0896-6273. doi: 10.1016/j.neuron.2018.10.049. URL http://dx.doi.org/10.1016/j.neuron.2018.10.049.

[81] James C Houk and Steven P Wise. Distributed modular architectures linking basal ganglia, cerebellum, and cerebral cortex: their role in planning and controlling action. *Cerebral cortex*, 5(2):95–110, 1995.

[82] F Middleton. Basal ganglia and cerebellar loops: motor and cognitive circuits. *Brain Research Reviews*, 31(2-3): 236–250, 3 2000. doi: 10.1016/s0165-0173(99)00040-5. URL http://dx.doi.org/10.1016/s0165-0173(99)00040-5.

[83] GW Arbuthnott, NK MacLeod, DJ Maxwell, and AK Wright. Distribution and synaptic contacts of the cortical terminals arising from neurons in the rat ventromedial thalamic nucleus. *Neuroscience*, 38(1):47–60, 1990.

[84] Eriko Kuramoto, Takahiro Furuta, Kouichi C. Nakamura, Tomo Unzai, Hiroyuki Hioki, and Takeshi Kaneko. Two types of thalamocortical projections from the motor thalamic nuclei of the rat: A single neuron-tracing study using viral vectors. *Cerebral Cortex*, 19(9):2065–2077, January 2009. ISSN 1047-3211. doi: 10.1093/cercor/bhn231. URL http://dx.doi.org/10.1093/cercor/bhn231.

[85] Eriko Kuramoto, Sachi Ohno, Takahiro Furuta, Tomo Unzai, Yasuhiro R. Tanaka, Hiroyuki Hioki, and Takeshi Kaneko. Ventral medial nucleus neurons send thalamocortical afferents more widely and more preferentially to layer 1 than neurons of the ventral anterior–ventral lateral nuclear complex in the rat. *Cerebral Cortex*, 25(1):221–235, August 2013. ISSN 1047-3211. doi: 10.1093/cercor/bht216. URL http://dx.doi.org/10.1093/cercor/bht216.

[86] Pablo Rubio-Garrido, Flor Pérez-de Manzo, César Porrero, Maria J. Galazo, and Francisco Clascá. Thalamic input to distal apical dendrites in neocortical layer 1 is massive and highly convergent. *Cerebral Cortex*, 19(10):2380–2395, February 2009. ISSN 1047-3211. doi: 10.1093/cercor/bhn259. URL http://dx.doi.org/10.1093/cercor/bhn259.

[87] Naoki Shigematsu, Yoshifumi Ueta, Alsayed A. Mohamed, Sayuri Hatada, Takaichi Fukuda, Yoshiyuki Kubota, and Yasuo Kawaguchi. Selective thalamic innervation of rat frontal cortical neurons. *Cerebral Cortex*, 26(6):2689–2704, June 2015. ISSN 1460-2199. doi: 10.1093/cercor/bhv124. URL http://dx.doi.org/10.1093/cercor/bhv124.

[88] John C Tuthill and Eiman Azim. Proprioception. *Current Biology*, 28(5):R194–R203, 2018.

[89] Floyd Ratliff, BW Knight, Jun-ichi Toyoda, and HK Hartline. Enhancement of flicker by lateral inhibition. *Science*, 158 (3799):392–393, 1967.

[90] Camila S. Deolindo, Ana C. B. Kunicki, Maria I. da Silva, Fabricio Lima Brasil, and Renan C. Moioli. Neuronal assemblies evidence distributed interactions within a tactile discrimination task in rats. *Frontiers in Neural Circuits*, 11, January 2018. ISSN 1662-5110. doi: 10.3389/fncir.2017.00114. URL http://dx.doi.org/10.3389/fncir.2017.00114.

[91] Vitor Lopes-dos Santos, Sergio Conde-Ocazionez, Miguel A. L. Nicolelis, Sidarta T. Ribeiro, and Adriano B. L. Tort. Neuronal assembly detection and cell membership specification by principal component analysis. *PLoS ONE*, 6(6): e20996, June 2011. ISSN 1932-6203. doi: 10.1371/journal.pone.0020996. URL http://dx.doi.org/10.1371/journal.pone.0020996.

[92] Eleonora Russo and Daniel Durstewitz. Cell assemblies at multiple time scales with arbitrary lag constellations. *Elife*, 6:e19428, 2017.

[93] Yoshio Sakurai. The search for cell assemblies in the working brain. *Behavioural Brain Research*, 91(1-2):1–13, 3 1998. doi: 10.1016/s0166-4328(97)00106-x. URL http://dx.doi.org/10.1016/s0166-4328(97)00106-x.

[94] Joseph Cichon and Wen-Biao Gan. Branch-specific dendritic ca2+ spikes cause persistent synaptic plasticity. *Nature*, 520 (7546):180–185, March 2015. ISSN 1476-4687. doi: 10.1038/nature14251. URL http://dx.doi.org/10.1038/nature14251.

[95] Chi Ren, Kailong Peng, Ruize Yang, Weikang Liu, Chang Liu, and Takaki Komiyama. Global and subtype-specific modulation of cortical inhibitory neurons regulated by acetylcholine during motor learning. *Neuron*, 110(14):2334–2350.e8, July 2022. ISSN 0896-6273. doi: 10.1016/j.neuron.2022.04.031. URL http://dx.doi.org/10.1016/j.neuron.2022.04.031.

[96] Naiyan Chen, Hiroki Sugihara, and Mriganka Sur. An acetylcholine-activated microcircuit drives temporal dynamics of cortical activity. *Nature Neuroscience*, 18(6):892–902, April 2015. ISSN 1546-1726. doi: 10.1038/nn.4002. URL http://dx.doi.org/10.1038/nn.4002.

[97] Michael Goard and Yang Dan. Basal forebrain activation enhances cortical coding of natural scenes. *Nature Neuroscience*, 12(11):1444–1449, October 2009. ISSN 1546-1726. doi: 10.1038/nn.2402. URL http://dx.doi.org/10.1038/nn.2402.

[98] Joshua Obermayer, Tim S. Heistek, Amber Kerkhofs, Natalia A. Goriounova, Tim Kroon, Johannes C. Baayen, Sander Idema, Guilherme Testa-Silva, Jonathan J. Couey, and Huibert D. Mansvelder. Lateral inhibition by martinotti interneurons is facilitated by cholinergic inputs in human and mouse neocortex. *Nature Communications*, 9(1), October 2018. ISSN 2041-1723. doi: 10.1038/s41467-018-06628-w. URL http://dx.doi.org/10.1038/s41467-018-06628-w.

[99] Mahesh M Karnani, Masakazu Agetsuma, and Rafael Yuste. A blanket of inhibition: functional inferences from dense inhibitory connectivity. *Current Opinion in Neurobiology*, 26: 96–102, June 2014. ISSN 0959-4388. doi: 10.1016/j.conb.2013.12.015. URL http://dx.doi.org/10.1016/j.conb.2013.12.015.

[100] Margaret Y Mahan and Apostolos P Georgopoulos. Motor directional tuning across brain areas: directional resonance and the role of inhibition for directional accuracy. *Frontiers in neural circuits*, 7:92, 2013.

[101] Apostolos P Georgopoulos and Adam F Carpenter. Coding of movements in the motor cortex. *Current opinion in neurobiology*, 33:34–39, 2015.